Photonic light trapping and electrical transport in thin-film silicon solar cells

Lucio Claudio Andreani *, Angelo Bozzola, Piotr Kowalczewski, Marco Liscidini

Department of Physics and CNISM, University of Pavia, via Bassi 6, I-27100 Pavia, Italy

ARTICLE INFO

ABSTRACT

Efficient solar cells require both strong absorption and effective collection of photogenerated carriers. With these requirements in mind, the absorber layer should be optically thick but electrically thin, to benefit from reduced bulk transport losses. It is therefore important to clarify whether thin-film silicon solar cells can compete with conventional wafer-based devices. In this paper we present a theoretical study of optical and electro-optical performance of thin-film crystalline silicon (c-Si) solar cells implementing light-trapping schemes. First, we use Rigorous Coupled-Wave Analysis (RCWA) to assess the light-trapping capabilities of a number of photonic structures characterized by different levels of disorder. Then, we present two approaches for electro-optical modeling of textured solar cells: a simplified analytic model and a numerical approach that combines RCWA and the Finite-Element Method. We consider both bulk and surface recombination in solar cells with the absorber thickness ranging from 1 to 100 µm. Our results predict that with state-of-the-art material quality of thin c-Si layers, the optimal absorber thickness is of the order of tens of microns. Furthermore, we show that thin-film solar cells with realistic material parameters can outperform bulk ones, provided surface recombination is below a critical value, which is compatible with present-day surface passivation technologies. This gives prospects for high-efficiency solar cells with much smaller c-Si thickness than in present wafer-based ones.

1. Introduction

Silicon solar cells have a significant potential for large-scale exploitation, as they are based on an abundant and non-toxic material. In recent years, the reduction of the fabrication cost was a driving force to develop solar cells with a micron-scale absorbing layer. Thin-film solar cells were mainly based on amorphous (a-Si), micro-crystalline (µc−Si) or nanocrystalline (nc-Si) silicon. Moreover, a number of groups have demonstrated multi-junction devices [1–3]. Yet, poor electrical transport properties of these materials remained a major roadblock in achieving high energy conversion efficiency. Therefore, lower material costs were obtained at the expense of lower efficiencies.

Recently, this picture has been changed: progress in the fabrication of thin epi-free c-Si layers [4] and thin multicrystalline Si on glass by liquid-phase recrystallization [5,6] gives the possibility to obtain high-quality thin silicon layers and solar cells with a promising efficiency [7,8]. Moreover, the recent drop in prices of conventional c-Si technologies mitigated the need for a reduction of the active material (and, hence, material costs). Instead, this trend suggests that *high efficiency* is now the key to lower the levelized cost of photovoltaic electricity (LCOE).

Thin-film technologies can reach high efficiency, provided that the thin absorbing layer is optically thick and electrically thin at the same time. While this paradigm is intrinsically satisfied in III–V semiconductors [9,10], CIGS [11,12], and, more recently, in perovskite compounds [13,14], the situation is more challenging in crystalline silicon. Therefore, high-efficiency thin-film c-Si solar cells require the implementation of broad-band *photonic structures* that are able to trap light and to enhance optical absorption in the thin absorber [15–31].

In this work we are going to address the following questions:

(1) What are the efficiency limits of realistic c-Si solar cells, compatible with present-day fabrication techniques?
(2) What are the solar cell structures that allow approaching these limits?

To answer these questions, it is helpful to explicitly formulate three basic ingredients of high-efficiency thin-film solar cells: (i) increasing optical absorption, which is usually evaluated with respect to the Lambertian limit [32–35]; (ii) maintaining a good carrier collection efficiency, especially in the presence of photonic structures, which may constitute a source of non-radiative (surface)

* Corresponding author.Tel.: +39 0382 987491; fax: +39 0382 987563.
E-mail address: lucio.andreani@unipv.it (L.C. Andreani).

recombination; (iii) reducing parasitic losses due to absorption in non-active layers, e.g., transparent conductive oxide (TCO) layer or a metal back-reflector. In this regard, an electro-optical modeling allows one to design solar cells that simultaneously meet these criteria [36–41].

In this contribution, we present an overview of the theoretical work performed at the University of Pavia, concerning light trapping and electrical transport in thin-film c-Si solar cells with light-trapping schemes. In this work we address issues (i) and (ii), while we disregard parasitic losses due to the TCO, assuming that they can be reduced to a negligible level or that the TCO can be replaced by low-loss metallic contacts. Anyway, including TCO-related losses would not change the trends as a function of thickness and the design of high-efficiency structures.

In the first part of this contribution, we aim at designing photonic structures to approach the Lambertian limit of absorption. In the second part of this paper we estimate the efficiency limits of thin-film c-Si solar cells with realistic assumptions for non-radiative recombinations. Here, we pay a particular attention to surface recombination, which is expected to play a major role in thin-film textured solar cells.

We describe two frameworks to study the electro-optical performance of textured solar cells: a simplified analytic model and a numerical approach, combining Rigorous Coupled-Wave Analysis (RCWA) and Finite-Element Method (FEM). Despite its simplicity, the analytical model captures the essential device physics. Therefore, in many cases this simple approach allows one to reach the same conclusions as more demanding numerical simulations.

In the FEM calculations we use a few well-justified simplifications, which allow to perform rigorous calculations at a significantly reduced computational cost. For example, we study two-dimensional (2D) solar cell structures with one-dimensional (1D) roughness, yet isotropy of the rough textures allows us to generalize the results to three-dimensional (3D) systems with 2D roughness. Therefore, we are able to efficiently analyze a wide range of material parameters.

The results of this paper go beyond our recently published ones [42,43], as we compare analytic and numerical treatments for the case of a rough interface, while comparison in Ref. [42] was done assuming an ideal Lambertian scatterer. The procedure extends the applicability of the analytic model to a wide class of solar cells with light-trapping schemes.

The idea of 1D or 2D photonic structures for light trapping in thin-film silicon layer is closely related to the concept of photonic crystal (PhC) slabs, as the increase of absorption follows partly from the coupling of the incoming light to the quasi-guided modes of such waveguide-embedded PhC structures. It is interesting to notice the analogy to other out- and in-coupling problems involving PhC slabs. For example, enhancement of light extraction from light-emitting devices (LEDs) can be achieved by using PhC structures, which recently allowed the realization of a PhC assisted Si LED [44]. Similarly, PhC structures have been designed to enhance nonlinear optical processes in PhC cavities [45]. Moreover, 2D polarization-diversity gratings are used to efficiently couple light from a single-mode optical fiber into a silicon photonic waveguide [46,47]. All these problems are physically analogous to light trapping in PV cells, as they involve coupling of light in the far field into (or from) a planar silicon slab. Yet, they are different in terms of the spectral region of interest. This analogy, which will not be pursued further in this paper, is an example of cross-fertilization between apparently different areas in photonics.

The rest of this paper is organized as follows: In Section 2 we discuss the Lambertian light trapping in thin-film solar cells, focusing on the dimensionality of photonic structures (1D vs. 2D).

In Section 3 we present the results of the optical calculations for ordered and partially disordered photonic structures. In Section 4 we analyze the optical performance of fully disordered photonic structures with randomly rough interfaces. In Section 5 we discuss the analytic and numerical frameworks used to study the electrical transport in solar cells with photonic structures. Here, we pay a particular attention to the dependence of efficiency on the absorber thickness and on surface recombination. Section 6 summarizes the results and gives an outlook for future work.

For clarity to the reader, we recall here the theoretical methods used in this work: analytic treatment of the Lambertian scattering (Section 2); Rigorous Coupled Wave Analysis (RCWA) for the calculation of the optical properties of solar cells with photonic crystal patterns and rough interfaces (Sections 3 and 4); analytic solution of the 1D drift-diffusion equations for carrier transport in presence of light trapping (Section 5.2); and Finite-Element Method (FEM) for electrical transport (Section 5.3). Each framework is briefly illustrated in the corresponding section, and details are given in the referenced papers.

2. Light trapping with Lambertian scatterer

Assuming 100% carrier collection, the photocurrent density of a solar cell is calculated as

$$J_{ph} = e \int A(E)\phi_{AM1.5}(E)\,dE, \tag{1}$$

where $A(E)$ is the absorptance of the silicon layer (i.e., the spectrally resolved absorption probability), and $\phi_{AM1.5}$ is the photon flux corresponding to the AM1.5G solar spectrum. For a thickness d and an absorption coefficient $\alpha(E)$, neglecting reflection losses, the single-pass absorptance is simply given by $1 - \exp(-\alpha(E)d)$. Usually, solar cells have a metal back-reflector characterized by high reflectivity and low loss, which nearly doubles the optical path of light. To increase the optical path further, a photonic structure can be implemented into the device to provide light scattering. In this section we consider the case of a *Lambertian scatterer* at the front surface of the device: this configuration is sketched in Fig. 1a. Denoting the scattering angle (with respect to the surface normal) as θ, the Lambertian scattering is characterized by an angular intensity distribution (AID) that is proportional to $\cos(\theta)$. This characteristic dependence leads to the *equal brightness effects*: the scattering surface shows the same brightness when viewed under different angles. If light scattering occurs only along one direction (for example, the x direction of Fig. 1a), then we refer to this case as that of a 1D Lambertian scatterer. If, instead, light is scattered along both x and y directions, we talk about 2D Lambertian scattering. The AID for these two cases may be written as

$$AID_{(1D)} = \frac{1}{2}\cos\theta, \tag{2}$$

$$AID_{(2D)} = \frac{1}{\pi}\cos\theta, \tag{3}$$

where the pre-factors take into account the normalization of the AID over a hemisphere. In the rest of this section, we assume the ray-optics regime, which is equivalent to saying that the optical density of states (DOS) in the absorber is the same as that in the bulk medium. Of course, this may not be the case for thin-film solar cells, when the thickness is of the order of or slightly larger than the wavelength of visible light. In this case, the high-index absorber may act as a waveguide and induce separate photonic bands in the optical DOS. The effects of optical confinement on the ultimate absorption limit have been treated by other authors [48]: here we choose to neglect such effects to arrive at a unified
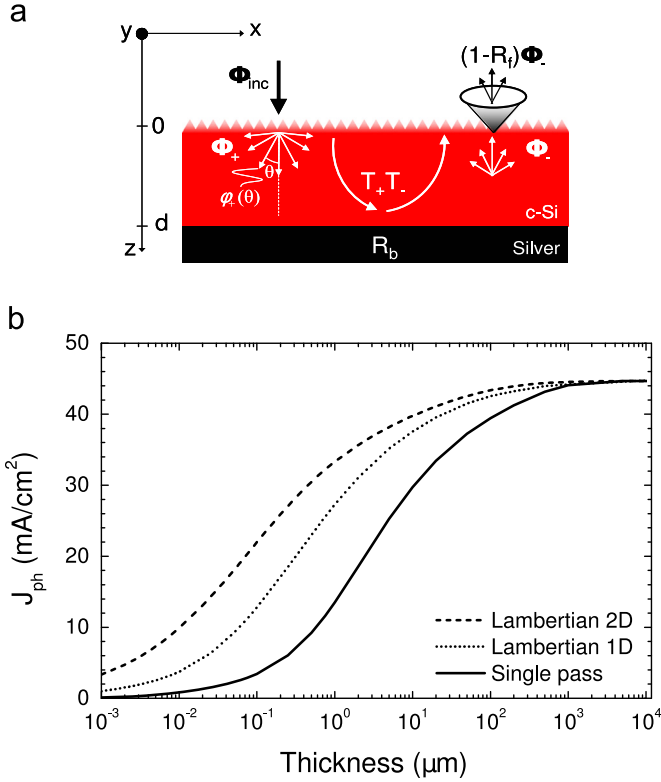
a

b

Fig. 1. (a) Sketch of a crystalline silicon solar cell with a Lambertian scatterer on the front surface. (b) Photocurrent density for c-Si solar cells as a function of the film thickness, under AM1.5 solar spectrum. The solid line refers to single-pass absorption; the dotted line refers to the 1D Lambertian limit, and the dashed line refers to the 2D Lambertian limit (see text). In all cases, reflection losses are not considered.

framework for both thin and thick layers. The wavelength-scale effects will be investigated in Sections 3 and 4, which focus on thin-film solar cells with photonic patterns.

As it was shown by Yablonovitch [32], inserting the Lambertian scatterer on the top (and/or on the rear) surface leads to complete randomization of the propagation angle of light, and it increases the optical path by a factor $4n^2$. This argument holds in the limit of very low absorption.

The generalization of the Lambertian scattering argument to the case of arbitrary absorption has been worked out by Green [33]. Following this treatment, the propagation of light inside the absorber is described by means of two hemispherical fluxes $\Phi_+(z)$ and $\Phi_-(z)$ (Fig. 1a). We use capital letters to denote the fluxes integrated over a hemisphere, and lower cases $\phi_+(z,\theta)$ and $\phi_-(z,\theta)$ to denote the specific angular contribution to the scattered intensity. If γ is the azimuth angle, the relation between ϕ and Φ fluxes can be written as

$$\Phi(z) = \int_{-\pi/2}^{\pi/2} \phi(z,\theta)\, d\theta, \tag{4}$$

$$\Phi(z) = \int_0^{2\pi} d\gamma \int_0^{\pi/2} \phi(z,\theta) \sin\theta\, d\theta, \tag{5}$$

for 1D and 2D Lambertian scattering, respectively.

Each angular contribution $\phi(z,\theta)$ experiences an optical path enhancement equal to $1/\cos\theta$, and it is attenuated during the propagation. In terms of integrated fluxes, it is useful to define the *total transmittance* T_+T_-, which links the hemispherical fluxes at the top surface ($z=0$):

$$\Phi_-(z=0) = T_+T_-\Phi_+(z=0). \tag{6}$$

Taking into account Eqs. (2)–(5) and defining the unpolarized silicon/silver back reflectance as $R_b(\theta)$, the total transmittance can be expressed as

$$T_+T_- = \frac{\int_{-\pi/2}^{\pi/2} \mathrm{AID_{1D}}\, e^{-2\alpha d/\cos\theta} R_b(\theta)\, d\theta}{\int_{-\pi/2}^{\pi/2} \mathrm{AID_{1D}}\, d\theta}$$

$$T_+T_- = \frac{\int_0^{\pi/2} \mathrm{AID_{2D}}\, e^{-2\alpha d/\cos\theta} R_b(\theta) \sin\theta\, d\theta}{\int_0^{\pi/2} \mathrm{AID_{2D}} \sin\theta\, d\theta}, \tag{7}$$

for 1D and 2D scattering, respectively. (Notice a missing factor 2 in the exponent of Eq. (8), Ref. [49].) From Eqs. (6) and (7) we can calculate the effective *optical path enhancement* averaged over all propagation directions as

$$d_{\mathrm{opt}}/d = -\frac{1}{2\alpha d}\ln(T_+T_-).$$

This quantity will be used in Section 5 when dealing with the carrier generation rate in the analytic model for transport.

Assuming that all the incident light is transmitted into the absorber without reflection losses, the absorption in silicon can be calculated as

$$A = \frac{1 - T_+T_-}{1 - R_f T_+T_-}, \tag{8}$$

where R_f denotes the fraction of the upward flux that is trapped inside the silicon absorber by total internal reflection (TIR). This quantity is equal to $1 - 1/n$ for 1D scattering and to $1 - 1/n^2$ for 2D scattering, where n is the real part of the refractive index of c-Si.

The resulting photocurrents in the case of crystalline silicon are shown in Fig. 1b as a function of the film thickness. The single pass case is reported with a solid line, while 1D and 2D Lambertian scattering limits are shown using a dotted and a dashed line, respectively. Achieving a J_{ph} higher than 40 mA/cm^2 (i.e., within ∼90% of the maximum value) requires c-Si thickness larger than 100 µm for single pass absorption, while a few µm thickness of c-Si are sufficient when 2D Lambertian light scattering is implemented. Fig. 1b – and the analogous ones for other common PV materials [50] – shows the potential of light trapping for reducing the PV material thickness and therefore the cost. More importantly, under the assumption that material quality is independent of thickness, the conversion efficiency of a thin-film solar cell can be higher than that of its thicker counterpart, due to more efficient collection of the photogenerated carriers in thinner layers. However, this conclusion may only hold if surface recombination processes can be neglected, or at least if they remain below a critical level. This crucial issue is discussed in Section 5 of this paper.

The curve for 2D scattering in Fig. 1b is usually referred to as the *Lambertian limit for light trapping*. However, it is not an absolute limit, as it has been shown that absorption can surpass the values given in Fig. 1 at specific wavelengths [48,50]. Properly speaking, the values of the absorption and photocurrent in the presence of Lambertian light scattering are a *benchmark* rather than a limit. However, for the sake of simplicity, in this paper we shall adhere to the common practice in the literature and use the expression *Lambertian limit* without any further specification.

It should also be noticed that these results depend on the dimensionality of the system [49]. When the randomizing surface scatters only in 1D, the light path enhancement is lower than for 2D scattering, and it leads to the curve shown in Fig. 1b with a dotted line. Two main factors determine the performance gap between 1D and 2D scatterers: the effective optical path enhancement and TIR, which are less efficient in the 1D case. These effects are particularly important in the infrared spectral region above the silicon band gap (1.1 eV). This region of the solar spectrum is rich of photons, and this amplifies the difference between the 1D and

2D case. We should also emphasize that the curves in Fig. 1b do not take into account neither reflection losses, nor parasitic losses due to other absorbing layers (metal and TCO). In other words, the Lambertian limit is evaluated in the idealized situation in which all the photons enter the silicon layer and can only be absorbed there. Reflection losses are considered in the next sections, together with (small) losses in the silver back-reflector, while parasitic losses in the TCO are disregarded in this work.

To conclude, we note that the differences between the curves corresponding to light trapping and the single-pass case are larger for thicknesses ranging from a few hundreds of nm to a few microns [51], where there is a crossover between Ray and Wave Optics. This range of thickness is thus the most interesting one for investigating the light trapping properties of photonic patterns. However, to reach photocurrent $J_{ph} > 40$ mA/cm^2, a silicon thickness above 10 μm should be also considered when full light trapping is implemented.

3. Photonic lattices: ordered and with correlated disorder

In this section we present the main results concerning crystalline silicon solar cells with photonic crystal structures for light trapping. The aim of this analysis is to optimize selected photonic configurations, and to derive easy guidelines that can be used for the design of highly efficient light trapping structures for thin-film devices.

The optical properties of photonic devices are calculated using the RCWA method [52,53]. This treatment, which belongs to a wider class of Fourier-modal methods, relies on the numerical solution of the Maxwell equations on a basis of plane wave states in each 2D layer. It is particularly suited for periodic systems, whose symmetry properties can be exploited to obtain a reliable description of the structure, provided that the basis set contains enough plane waves. The issue of numerical convergence and accuracy of the results is treated in detail in Refs. [49,50].

We start our investigation with simple 1D gratings made of parallel trenches of width b and 2D square lattices of holes with radius r etched into the silicon film. These structures are sketched in the insets of Fig. 2a and b, respectively. They can be fabricated using, for example, UV lithography [54] or nano-imprinting techniques [55], the latter being particularly promising for large scale applications.

Optical data for c-Si are taken from Palik, Ref. [56]. The silicon thickness d is varied from 250 nm to 4 μm, consistently with the conclusions of the previous section. We assume a semi-infinite silver [56] back reflector, and a 70 nm thick AR coating made of a transparent dielectric material with $n=1.65$. The same material fills the ridges and holes. The period Λ of the patterns shown in Fig. 2 is comparable with the useful wavelengths of the solar spectrum. This provides the additional wave vector components that are necessary for coupling light into the quasi-guided modes supported by the solar cells.

To elucidate this mechanism, in Fig. 2a and b we focus on the optimization of 1D and 2D patterns for the case of a 1 μm thick c-Si absorber. The optimization is performed by varying simultaneously the main lattice parameters: period (Λ), etching depth h, and dielectric material's fractions (b/Λ and r/Λ). In Fig. 2 we report the results for the optimal periods: $\Lambda=500$ nm for the 1D grating and $\Lambda=600$ nm for the 2D grating. The optimal configurations are characterized by a shallow etching depth (240 nm), and by similar optimal dielectric fractions around 30% (vertical axis of Fig. 2). The optimized gratings exhibit a geometric surface area enhancement (compared to a flat device) of the order of 1.6–1.7. This is an important parameter for electro-optical modeling, and it
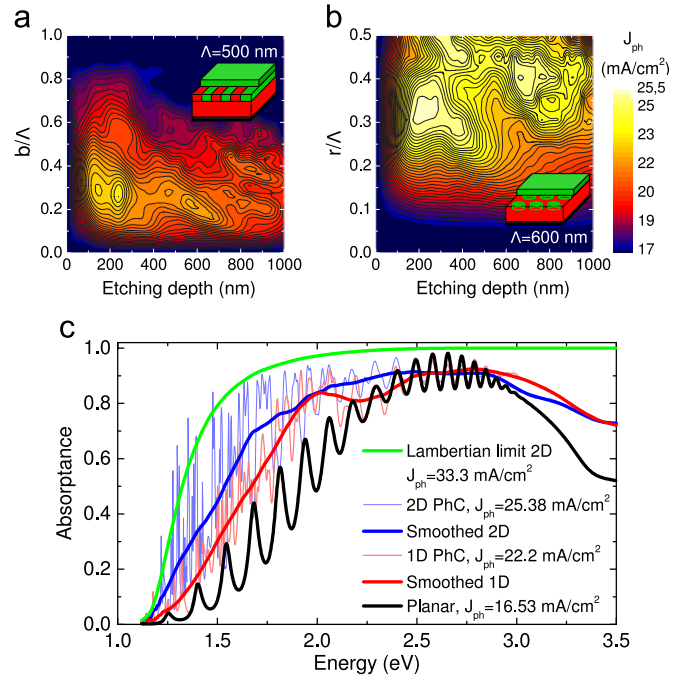

Fig. 2. Photocurrent density J_{ph} for 1 μm thick c-Si solar cells with 1D (a) and 2D (b) photonic structures as a function of etching depth and dielectric fractions. The width of the parallel trenches in (a) is denoted with b, the hole radius in (b) with r, and the lattice period with Λ. The optimal lattice periods are also reported in the contour plots. (c) Absorptance spectra for 1 μm thick c-Si solar cells: 2D Lambertian limit (green line), optimized 2D lattice with smoothed spectrum (thin and thick blue lines, respectively), optimized 1D grating with smoothed spectrum (thin and thick red lines, respectively), and flat reference cell (black line). (For interpretation of the references to color in this figure caption, the reader is referred to the web version of this paper.)

will be relevant in Section 6 when discussing the effects of the surface recombination.

The 2D lattice overcomes the 1D grating, with maximum J_{ph} of 25.38 and 22.2 mA/cm^2, respectively. The reason is that 2D symmetry provides more diffraction channels, thus more light can be coupled into the active layer. This aspect is analyzed in terms of the absorptance spectra shown in Fig. 2c. Here we report the curves for the optimal 1D and 2D configurations with thin blue and red lines, respectively. We also show the smoothed spectra as guides for the eye (thick blue and red lines), the 2D Lambertian limit for 1 μm c-Si (green line), and the absorptance for a flat device with the same 70 nm thick AR coating (black line).

We see that the photonic structures have two beneficial effects: (i) reflection losses are reduced, and (ii) the absorption at low energy is substantially increased. The first aspect can be qualitatively explained using effective index arguments [57,58]. Indeed the effective refractive index of the patterned region is intermediate between those of the AR material and c-Si. This gradual transition improves the impedance matching compared to the flat case (black line in Fig. 2c). Yet, it should be emphasized that, since the lattice period and all the other lattice feature sizes are comparable with the wavelengths of sunlight, we are not strictly in the range of validity of any effective medium theory [59,60], and this explanation is simply qualitative. Rigorous theoretical treatments, such as Fourier modal methods (as adopted here), finite-difference time-domain methods, and Finite-Elements Methods, have to be used for a quantitative evaluation of the active absorption and the corresponding photocurrent [57,58].

This analysis reveals the peculiar effect of periodic photonic structures, namely sharp peaks in the absorptance spectra, which
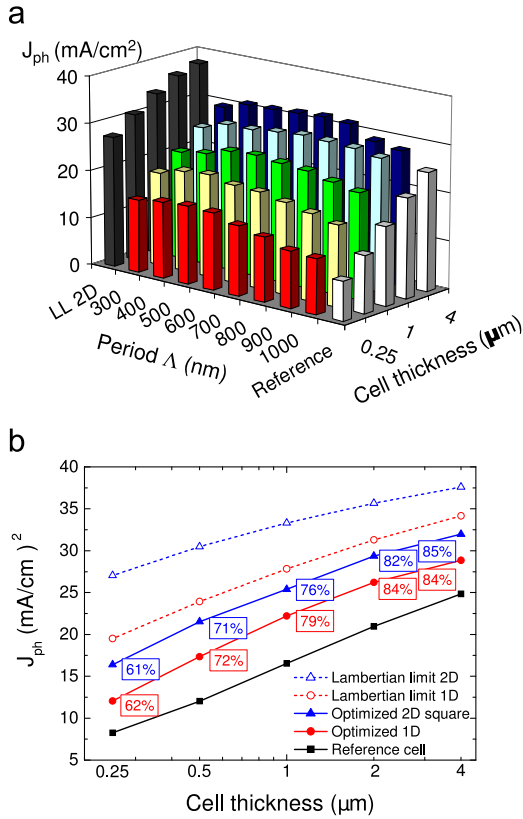
Fig. 3. (a) Photocurrent density J_{ph} for c-Si solar cells with 2D photonic patterns with different lattice periods Λ and cell thickness d. For each couple of Λ and d, the hole radius and the etching depth are optimized to maximize the photocurrent. (b) Photocurrent density for 1D and 2D Lambertian limits (dashed red and blue lines, respectively), for 1D and 2D optimized photonic structures (solid red and blue lines respectively), and for the reference flat cell (black solid line) as a function of the silicon thickness. (For interpretation of the references to color in this figure caption, the reader is referred to the web version of this paper.)

Fig. 4. (a) Sketch of a 1 μm thick silicon solar cell with a front 1D grating with size and position disorder. The supercell period $\Lambda = 5$ μm is also reported. (b) Average photocurrent density for solar cells with uncorrelated Gaussian disorder for the width σ_w and position σ_x of the silicon ridges. (c) Best J_{ph} for solar cells with correlated Gaussian disorder as a function of σ_a. The values for the 1D Lambertian limit, for the best ordered grating, and for the reference flat cells are reported with horizontal lines.

are due to the coupling of the incident light into the guided modes of the structure.

In Fig. 3a we report the photocurrent density of 2D gratings as a function of the cell thickness and the lattice period. For each couple of parameters, the etching depth and the AR material fraction have been optimized to maximize J_{ph}. When the cell thickness is increased, the spectral range for light trapping moves to lower energies. To maximize forward diffraction into the active material, the lattice period has to be increased consequently. This trend is evident in Fig. 3a, where the optimal Λ increases from 500 nm for a 250 nm thick c-Si solar cell to 700 nm for a 4 μm thick cell.

The maximum values of J_{ph} obtained for each silicon thickness are reported in Fig. 3b for 1D and 2D gratings (red and blue solid lines, respectively). We also show the curves for the cases of 1D and 2D Lambertian light trapping (red and blue dashed lines, respectively) and for the flat device with an optimized AR coating (black solid line). The fraction of the corresponding Lambertian limit achieved with the optimized photonic structures is also reported. In agreement with the preliminary analysis of Section 2, we observe that photonic light trapping boosts the absorption in the whole thickness range, and its importance increases in very thin films. After the optimization of the photonic structures, 1D and 2D gratings reach substantially the same fraction of the corresponding limits. This is a further confirmation that the unified theoretical framework of Section 2 correctly reproduces all the optical effects induced by the different dimensionality of the photonic structures.

Remarkably, the Lambertian limit can be overcome at specific wavelengths, as shown in Fig. 2c. However, when we look at the
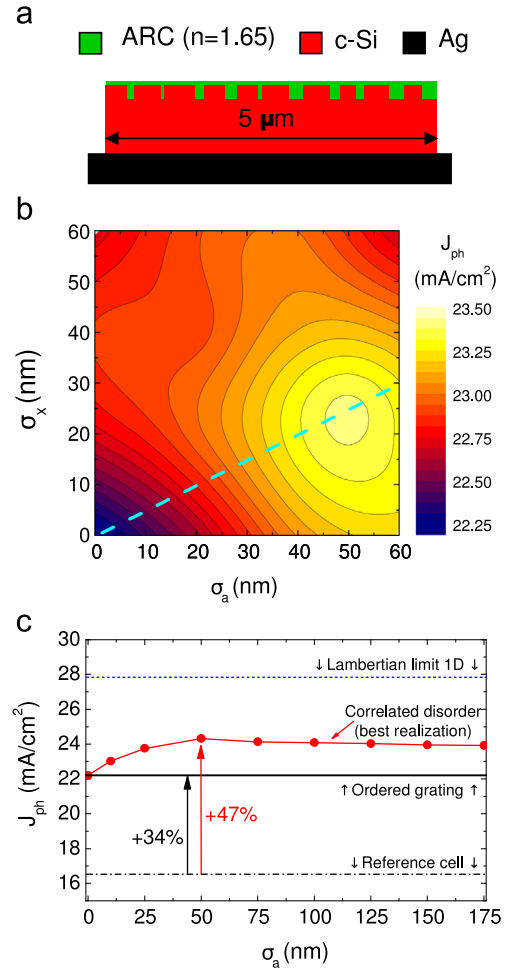
integrated photocurrent of Fig. 3b, the values corresponding to 1D and 2D structures are still intermediate between the Lambertian limit and the flat reference case. To bring the absorption to the ultimate limit, different photonic structures have to be employed.

For this purpose, we focus on the mechanism of coupling light into the quasi-guided modes, and we try to improve its efficiency over a broader spectral range [49]. The main limitation of ordered structures is the number of diffraction channels that can be exploited for coupling. At the optimal period ($\Lambda \simeq 500$–600 nm), no more than 1–2 diffraction orders are available for coupling in the near infrared. In this range, resonances are very sharp, but the absorption cross section of the single peak is rather small (Fig. 2c). To improve light coupling, we propose to enrich the Fourier spectrum of the photonic structures by including a controlled amount of disorder into the optimal 1D ordered configuration of Fig. 2c (red lines). Disorder is modeled in the RCWA formalism using a supercell approach [49]. We focus on 1D structures with a 5 μm wide supercell containing 10 dielectric ridges. A scheme of the supercell is reported in Fig. 4a. We assume that size and position of the silicon ridges are characterized by Gaussian distributions, with standard deviations σ_w and σ_x, respectively. The mean size of the silicon ridges is 350 nm (which leads to a
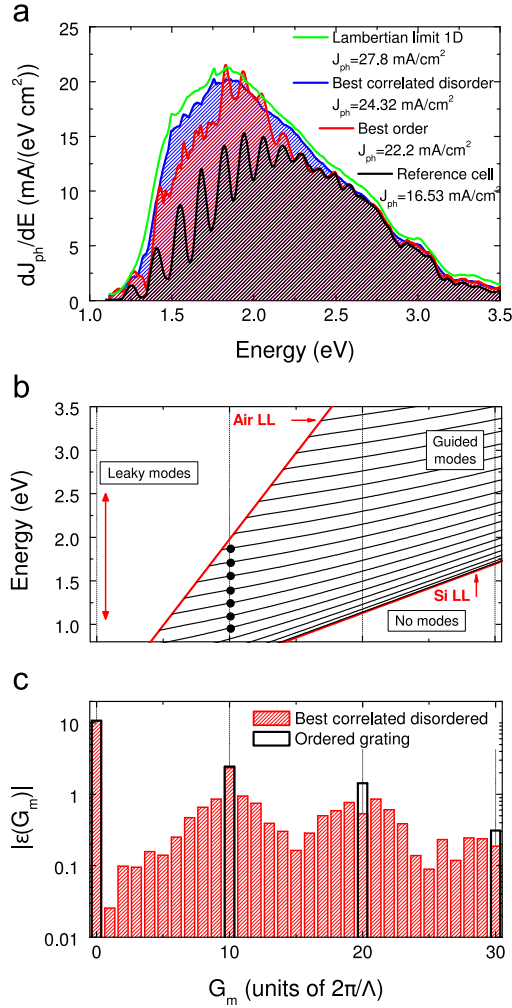
Fig. 5. (a) Spectral contributions to the photocurrent density for the 1D Lambertian limit (green line), for the best structure with correlated disorder (blue line), for the best 1D ordered grating (red line), and for the flat reference cell (black line). (b) TE guided modes for a free standing, 1 µm thick c-Si waveguide. Coupling mediated by the $m=10$ channel is represented with black dots. (c) Absolute values of the Fourier components of the dielectric function of patterned layers: ordered 1D grating (black bars) and best structure with correlated disorder (red bars). (For interpretation of the references to color in this figure caption, the reader is referred to the web version of this paper.)

silicon fill factor equal to 0.7), and the average positions are those of the previously optimized 1D ordered grating. The effects of disorder are analyzed calculating the photocurrent as a function of the two independent parameters σ_w and σ_x, as shown in Fig. 4b.

We find that the addition of disorder improves light harvesting. The photocurrent is always higher than that of the ordered configuration. The optimal configuration is neither perfectly ordered nor totally random, but actually contains a finite amount of disorder with $\sigma_x \sim 25$ nm and $\sigma_w \sim 50$ nm [49], as also found by other authors on related systems [61–65]. The photocurrent increases from 22.2 mA/cm^2 for the optimized simple grating to 23.4 mA/cm^2 for the best uncorrelated Gaussian disorder. The optimal configuration lies along the line $\sigma_x = \sigma_w/2$, which is reported in Fig. 4b with a dashed cyan line. To speed up the investigation of disorder and to have more chances to find the configurations characterized by the highest photocurrent, we introduce a correlated Gaussian disorder. This disorder is characterized by a single parameter $\sigma_a \equiv \sigma_w/f_{Si} = 2\sigma_x/f_{Si}$, where $f_{Si}=0.7$ is the fraction of silicon in the optimized 1D ordered grating. The same silicon fraction is assumed also for the partially

disordered gratings. Note that the single parameter σ_a takes into account the constraint $\sigma_w/\sigma_x = 2$ [49]. In Fig. 4c we report the photocurrent J_{ph} as a function of σ_a. The best correlated configuration corresponds to $\sigma_a = 75$ nm and $J_{ph} = 24.32$ mA/cm^2.

To prove that disorder leads to broad-band light harvesting, in Fig. 5a we report the spectral contributions to the photocurrent, which are obtained multiplying the calculated absorptance with the AM 1.5 photon flux. We see that the photonic crystal structures substantially improve light harvesting compared to the flat device (black line) for energies below 2.25 eV. The optimal ordered configuration (red line) shows prominent peaks and overcomes the 1D Lambertian limit (green line) at the coupling conditions. The condition of light coupling to the guided TE modes supported by a 1 µm silicon layer is illustrated in Fig. 5b. Here we assume the same supercell period $\Lambda = 5$ µm is adopted in Fig. 4a. The light coupling occurs at the intersection between the photonic bands and the vertical line denoting each Fourier component. The Fourier spectrum of the ordered grating is reported in Fig. 5c with black bars. In Fig. 5b we focus on the Fourier component $G_m = 10 \times 2\pi/\Lambda$ (black dots). Also higher order channels are active in the energy range where light trapping is needed (vertical arrow in Fig. 5b), with smaller strength. In this range, modes characterized by $m=20$ and 30 can couple light only into the modes close to the silicon light line. As also pointed out by other authors [66,62,63], these modes are strongly confined into the silicon layer and are difficult to excite with an incident plane wave. Modes close to the air light line are much easier to excite since evanescent tails extend further in air, providing a better field overlap with the incident field. Thus, the diffraction properties of ordered gratings rely mainly on the sole first diffraction order. This implies a limited width of each absorptance resonance, and a spectral contribution well below the Lambertian limit for energies below 1.75 eV (red curve in Fig. 5a).

Instead, the Fourier spectrum of the correlated disordered structure (red bars in Fig. 5c) is richer than that of the simple grating, and this is the key factor for higher photocurrent. In this system, there are more channels around the dominant one at $m=10$ that can be used for coupling. Thus, the Fourier components of the photonic patterns can be tailored to improve coupling to the guided modes between the gap and approximately 2 eV. This target region is denoted with a vertical red arrow in Fig. 5b. When the coupling strength is distributed over the channels around the $m=10$ order, the resonant peaks in the optical spectra are broadened. The absorption cross section is increased compared to the ordered configuration, as shown in Fig. 5a with a blue line. Remarkably, the system with correlated Gaussian disorder reaches 87% of the 1D Lambertian limit in terms of photocurrent. By taking into account the optimal correlation trend and the Fourier spectrum of photonic layers, we derive simple guidelines for the design of photonic structures with complicated unit cells [49]. Other 2D quasi-random structures with supercell designed to approach the 2D Lambertian limit have been recently proposed [63–65]. These important results can be explained adapting our analysis to 2D systems, and they are in line with our conclusion.

It should be noticed that our analysis could be applied to the design of photonic structures for the efficient extraction of light from thin light emitting devices. In the next section, we tackle the problem of efficient light trapping starting from systems characterized by rough scattering interfaces. Although such fully random systems could appear to be totally different from those considered in the present section, they can actually be viewed as a limiting case of correlated disorder, possibly with more complex (nonbinary) diffraction gratings. Thus, the approaches based on ordered photonic structures, correlated disorder, and full random structures, are conceptually linked to one another.
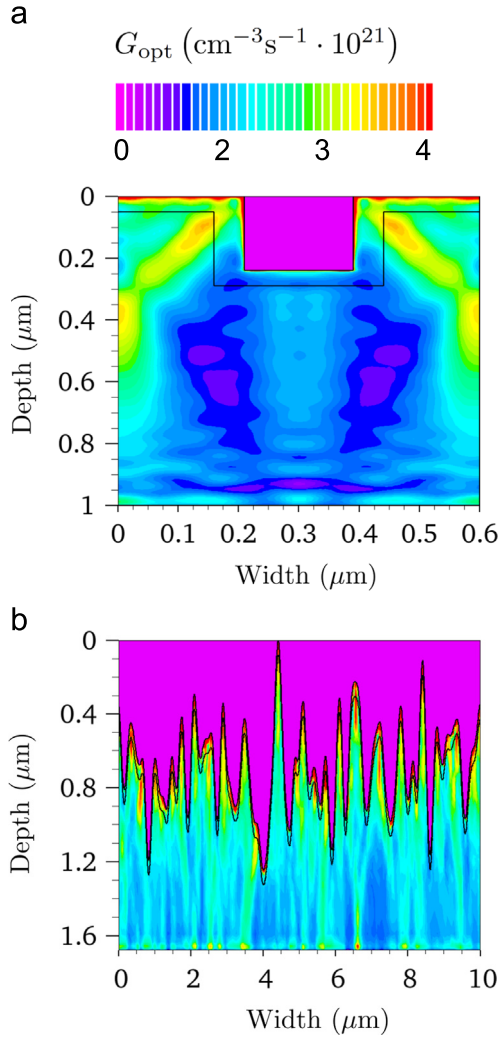
Fig. 6. Photogeneration rates calculated for structures with (a) grating and (b) rough texture, illustrating the difference between light-trapping mechanisms between diffractive and diffusive structures. The volume of the rough structure corresponds to the volume of 1 μm thick flat absorber. Violet regions above the textures correspond to anti-reflection coating/transparent front electrode. (For interpretation of the references to color in this figure caption, the reader is referred to the web version of this paper.)

4. Randomly rough and hybrid photonic structures

Another strategy to trap sunlight in a thin absorber layer is based on rough textures [29,67–69]. The light-trapping mechanism in this approach is different from that corresponding to the ordered and semi-ordered photonic lattices described previously. This difference is illustrated in Fig. 6: in the case of the structure with a diffraction grating the absorption is enhanced thanks to the guided modes of the absorber, and thus a mode pattern in the photogeneration profile can be easily recognized (a). On the contrary, light transmitted through a rough interface is diffused (b). This implies that (1) photogeneration profile is mainly due to random scattering, and does not exhibit any mode pattern; (2) rough textures are intrinsically broadband scatterers, which is a key requirement for photovoltaic applications.

We model rough interfaces by a Gaussian roughness, characterized by root mean square (RMS) deviation of height σ and lateral correlation length l_c. The algorithm used to generate randomly rough interfaces with a given σ and l_c was taken from [70]. We adopt again a supercell approach within the RCWA method: the supercell size is typically around 10 μm (convergence
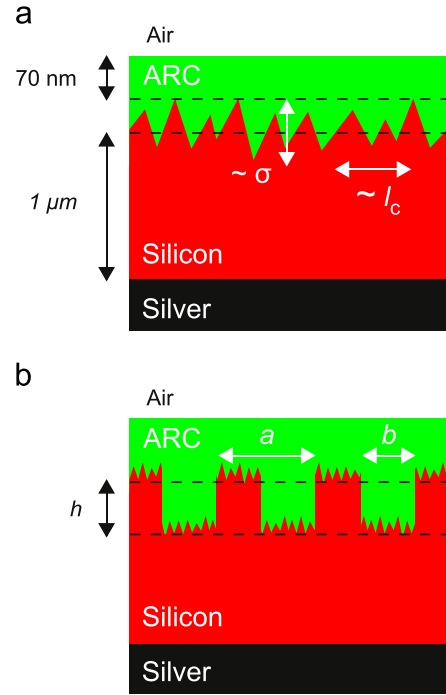

Fig. 7. (a) Thin-film solar cell with a randomly rough texture. The roughness is described by root-mean-square (RMS) deviation of height σ and lateral correlation length l_c. (b) Thin-film solar cell with a hybrid interface, being a combination of a rough interface and a diffraction grating. The grating is characterized by period a, width of the etched region b, and etching depth h.

was tested from 5 to 20 μm). Thus, the present approach is analogous to that adopted for treating correlated disorder in Section 3.

We benefit from the isotropy of the considered rough textures, which allows one to calculate the optical properties of 2D interfaces by averaging the results obtained for an ensemble of 1D rough surface realizations. A comparison with the calculations performed for measured rough surface topographies [71] confirmed that this simple model of roughness accurately describes the optical properties of common rough textures [72]. Therefore, this approach allows performing rigorous optical calculations at a significantly reduced computational cost.

The considered solar cell with a randomly rough texture is sketched in Fig. 7a. It consists of a 1 μm thick crystalline silicon absorber [56], 70 nm thick anti-reflection coating (ARC), and silver back reflector [56]. The ARC is transparent, with refractive index $n_{ARC} = 1.65$.

To maximize photocurrent generated in the structure shown in Fig. 7a, we calculate J_{ph} as a function of σ, from 0 to 300 nm, and l_c, from 60 and 220 nm. For different parameters of the rough interface, we keep the volume of silicon constant and equal to the volume corresponding to a 1 μm thick absorber with a flat ARC/Si interface. As shown in Fig. 8a, in the considered parameter range, J_{ph} depends mainly on σ, with a modest bell-like dependence on l_c. For l_c around 150 nm, J_{ph} saturates for σ larger than 200 nm, and only a modest photocurrent enhancement can be observed for larger roughness.

In Fig. 8a we also indicate the positions corresponding to the Neuchâtel and Asahi-U substrates, showing the possibility of improving light trapping by optimizing the roughness parameters. The photocurrent density in the structure with an optimized rough interface ($\sigma = 300$ nm, $l_c = 160$ nm) is 24 mA/cm^2, which corresponds to 94% of the 1D Lambertian limit [49]. Here, to provide an accurate comparison, reflection losses at the air/ARC interface were included in the Lambertian limit. To quantify the losses at the rear
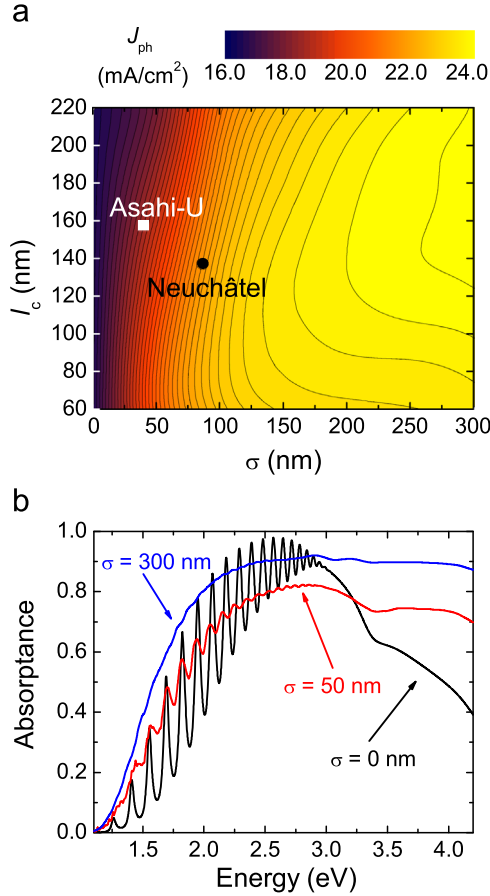
a

b

Fig. 8. (a) Photocurrent density as a function of lateral correlation length l_c and RMS deviation of height σ, calculated for 1 µm thick rough solar cell, sketched in Fig. 7a. Each point is calculated as an average of 10 surface realizations. (b) Absorptance corresponding to the 1 µm thick c-Si solar cell with random texture, which is characterized by three different values of σ. Lateral correlation length in all cases is equal to $l_c = 160$ nm.
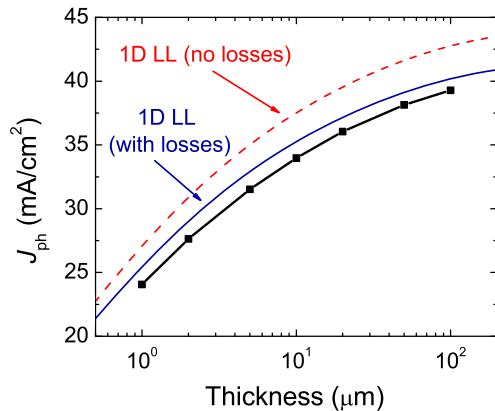

Fig. 9. Black symbols and connecting lines: J_{ph} as a function of the absorber thickness for the solar cells with the optimized random texture ($\sigma=300$ nm, $l_c = 160$ nm) and a silver back reflector. The results are compared with J_{ph} corresponding to the 1D Lambertian limit: the red dashed line denotes the 1D Lambertian limit assuming a perfect anti-reflection action; the blue solid line shows the 1D Lambertian limit including reflection losses (around 6%) at the air/ARC interface. (For interpretation of the references to color in this figure caption, the reader is referred to the web version of this paper.)

(silicon/silver) interface, we have also considered a structure with a perfect mirror instead of silver. In this case, $J_{ph} = 24.9$ mA/cm^2, which corresponds to 98% of the 1D Lambertian limit.

In Fig. 9 we show J_{ph} as a function of thickness for the c-Si solar cells with the optimized random texture ($\sigma=300$ nm, $l_c = 160$ nm)

and a silver back reflector. The results are compared with J_{ph} corresponding to the 1D Lambertian limit: the red dashed line denotes the 1D Lambertian limit assuming a perfect anti-reflection action (as in Fig. 1); the blue solid line shows the 1D Lambertian limit including reflection losses (around 6%) at the air/ARC interface. A comparison with the latter limit allows one to assess the light-trapping capabilities of random textures (as the texture cannot improve the anti-reflection action at the air/ARC interface). It can be seen that J_{ph} in textured cells can reach more than 94% of the Lambertian limit with reflection losses, regardless of the absorber thickness. The absorption in thicker cells is even closer to the Lambertian limit, because parasitic losses in the silver back reflector become less important for larger thickness.

First, we have optimized the parameters of the random texture for a single absorber thickness ($d = 1$ µm). Then, we used the same roughness parameters also for different thickness values. Our calculations show that the random texture with the same statistical parameters allows one to obtain approximately the same fraction of the Lambertian Limit regardless of the absorber thickness. (Actually, the fraction of the Lambertian limit increases from 94% to 98% when the thickness increases from 1 to 100 µm.) This suggests that the optimal parameters of the rough texture do not change significantly in the considered absorber thickness range. Therefore, we expect that any further optimization for different absorber thickness values may lead only to a minor improvement.

Fig. 8b gives an insight into the light-trapping mechanism corresponding to the optimized roughness. It shows the absorptance in the 1 µm thick c-Si solar cell with random textures, which are characterized by three different values of σ. The lateral correlation length in all cases is equal to $l_c = 160$ nm. For $\sigma=0$ nm, i.e., for the unstructured cell, one can easily recognize Fabry–Pérot oscillations in the thin film. For increasing σ, the oscillations are smoothed out by the roughness: for $\sigma=50$ nm the absorptance is increased, but the relative amplitude of the oscillations is smaller. Finally, for $\sigma=300$ nm there are no oscillations whatsoever; the roughness provides a broadband absorption enhancement in the whole spectral range. This confirms that the light-trapping mechanism for randomly rough solar cells is based on random scattering, rather than on resonances corresponding to guided modes.

Although the optimized rough interface performs very well from the optical point of view, obtaining photocurrent close to the Lambertian limit requires large and sharp surface features (i.e., large σ to l_c ratio). This may be impractical, as it may decrease the electrical quality of the whole solar cell structure. To address this problem, we study a hybrid interface [73], namely a combination of a shallow rough interface and a diffraction grating. This concept is an extension of the idea of a modulated surface texture [74], and it allows to obtain strong absorption enhancement using a rough interface with a modest feature size. A solar cell with the hybrid interface is sketched in Fig. 7b. We use the optimal parameters of the 1D grating for a 1 µm thick c-Si solar cell: period $a=600$ nm, width of the etched region $b=180$ nm, and etching depth $h=240$ nm [50]. Both the lateral and vertical features of the roughness are much smaller than those corresponding to the optimal rough interface: $\sigma=80$ nm, $l_c = 60$ nm.

Fig. 10 shows the absorptance calculated for 1 µm thick solar cells with an optimized diffraction grating, shallow roughness, and hybrid interface, the latter being a combination of both. Merging the diffraction grating with the shallow rough interface increases the absorption in the system, resulting in a redshift of the whole spectrum. As a result, the structure with the hybrid interface outperforms those with the optimized diffraction grating and with the shallow rough interface. Moreover, the spectral features corresponding to the grating are smoothed.

The absorptance in the structure with the hybrid interface is close to that in the structure with the optimized roughness, as shown in

Fig. 10. The photocurrent density in the structure with the hybrid interface is $J_{ph} = 23.7$ mA/cm². Achieving such a high J_{ph} in the structure with a rough interface would require $\sigma = 200$ nm. Therefore, the hybrid interface allows one to significantly reduce σ, with beneficial effects for the electrical quality of the silicon/oxide interface.

These results show that the concept of a hybrid interface is a promising route to achieve a broad-band absorption enhancement with a shallow roughness. However, we notice that the scattering
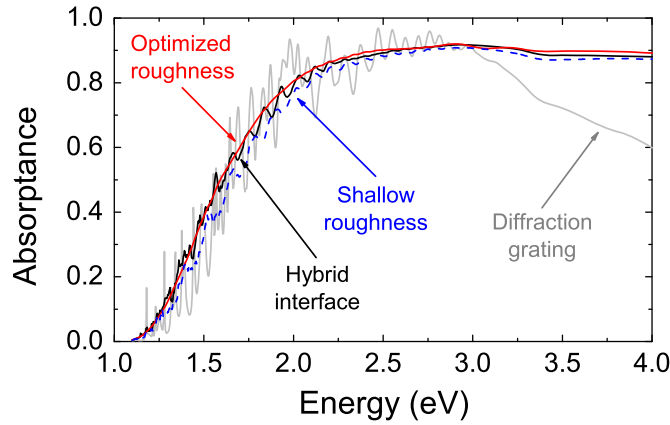

Fig. 10. Absorptance calculated for the 1 μm thick solar cells with an optimized diffraction grating, shallow roughness, and hybrid interface, being a combination of both. These results are compared with absorptance calculated for the structure with the optimal rough texture.
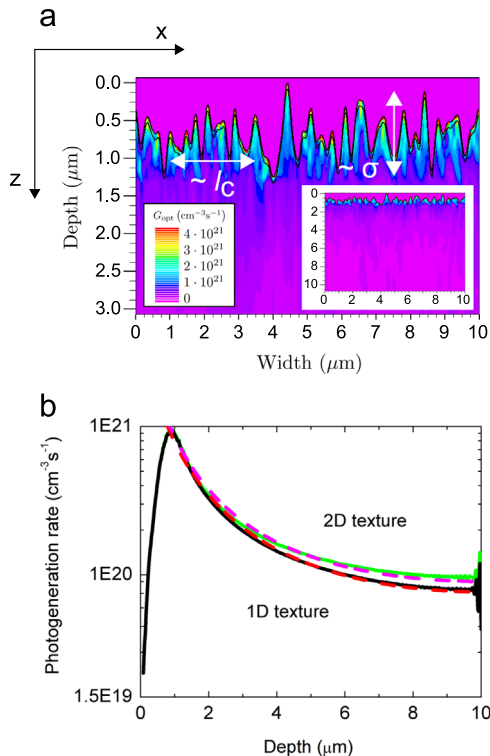

Fig. 11. (a) Photogeneration profile calculated for the 10 μm thick c-Si solar cell with a randomly rough texture. The roughness is described by the root-mean-square (RMS) deviation of height σ and the lateral correlation length l_c. The main plot shows the photogeneration profile close to the texture, whereas the inset shows the whole cell. Lengths in the inset are given in μm. (b) Photogeneration rate for a one-dimensional rough texture averaged over x direction (black solid line) compared with the corresponding one-dimensional Lambertian limit (red dashed line); rescaled photogeneration rate (green solid line) compared with the two-dimensional Lambertian limit (magenta dashed line). (For interpretation of the references to color in this figure caption, the reader is referred to the web version of this paper.)

properties of a hybrid interface are no longer isotropic. Thus, the connection between a one-dimensional model and the optical properties of a two-dimensional system in this case is not as straightforward as it is for isotropic rough interfaces. A generalization of the present concept to 2D rough structures with 2D photonic lattices is left for future work.

5. Electro-optical modeling

In this section we focus on the electro-optical modeling of thin-film silicon solar cells by solving the drift-diffusion equations for carrier transport for a given photogeneration rate profile. The goal is to calculate the energy conversion efficiency as a function of the absorber thickness in the range 1–100 μm with a photonic structure for the front interface that comes as close as possible to the Lambertian limit. Therefore, we choose the randomly rough interface with Gaussian disorder, which was shown in Section 4 to approach the Lambertian limit in the whole range of thicknesses. To solve drift-diffusion equations we adopt two approaches, namely an analytic model and a full numerical treatment based on FEM simulations. The details of the two approaches are presented in our recent works: the analytic model in Ref. [42] and the FEM simulations in Ref. [43]. The main novelty in this paper is that we compare the analytic and numerical treatments for the case of the rough surface (while comparison in Ref. [42] was done assuming an ideal Lambertian scatterer).

The strategy of this section is at follows: in Section 5.1 we first discuss the photogeneration rate profile that is used later as source term for the electro-optical modeling. In particular, we explain how the photogeneration rate calculated for the 1D Gaussian roughness model can be extrapolated to the case of 2D scattering, by using the Lambertian limit as a reference. In Section 5.2 we describe the analytic model for solving drift-diffusion equations, while in Section 5.3 we give a brief account of the numerical approach based on the FEM simulations. Finally, in Section 5.4 we present the results for the energy conversion efficiency of thin-film silicon solar cells as a function of the absorber thickness in the range 1–100 μm. We focus on the effects of nonradiative processes, namely bulk recombination (expressed by carrier diffusion lengths) and surface recombination (quantified by surface recombination velocity at front and rear surfaces). The goal is to determine the efficiency limits of thin-film c-Si solar cells, and to quantify the material quality and surface recombination that allow approaching these limits. The comparison between the analytic model and the numerical simulation approach is presented throughout, in order to provide a "stress test" for the analytic approach in a wide range of parameters.

5.1. Photogeneration profile

For the electro-optical modeling of thin-film solar cells, it is not only important *how much* light is absorbed, but also *where* the carriers are generated. An example of the photogeneration profile calculated for a 10 μm thick c-Si solar cell with randomly rough texture is shown in Fig. 11a. The main plot shows the photogeneration profile close to the texture, whereas the inset shows the whole cell. The photogeneration rate is integrated between 1.1 and 4.2 eV and averaged over both polarizations. There is no mode pattern present, which is a direct consequence of the dominating light-trapping mechanism, and confirms the analysis presented in Section 4.

The photogeneration profile shown in Fig. 11a is random. Yet, averaging over x direction and presenting the photogeneration rate as a function of depth, as shown in Fig. 11b, can reveal clear trends. The photogeneration rate corresponding to the 1D texture

(black solid line) initially increases (due to the increasing fraction of silicon), and then it decays exponentially. The decaying part can be fitted with the photogeneration rate corresponding to the 1D Lambertian scatterer (red dashed line).

So far, this analysis refers to a one-dimensional rough interface. Although the optical properties of two-dimensional textures are well reproduced by a one-dimensional model [72], a 1D texture scatters light only in a plane, thus it yields a lower photocurrent than for 2D scattering. To account for an increased number of diffraction channels, we use a simple rescaling procedure [43]. If the photogeneration rate corresponding to the 1D roughness is similar (except for the increasing part) to the photogeneration rate of the 1D Lambertian limit, it is justified to assume that the photogeneration rate for the two-dimensional isotropic rough interface with the same parameters is similar to the corresponding 2D Lambertian limit. Based on this assumption, we multiply the photogeneration rate calculated for a one-dimensional interface by the ratio of the absorptance calculated for the 2D Lambertian scatterer to the absorptance calculated for the 1D Lambertian scatterer. Such a scaling factor depends on energy and thickness of the absorber, yet it is independent of the position (x,z).

On the one hand, a complete rescaled photogeneration profile, as the one shown in Fig. 11a, will be used as an input for the numerical calculations. On the other hand, the normalized photogeneration rate corresponding to the 2D scatterer, denoted with magenta dashed line in Fig. 11b, will be used as an input for the analytical treatment. Despite this simplification, we will show that the analytical model captures the essential physics and agrees very well with the numerical calculations.

We emphasize that in the electrical calculations we use the complete photogeneration profile, as shown in Fig. 11a. The averaged profile, shown in Fig. 11b, is only to demonstrate the similarities with the Lambertian photogeneration rate.

In this work we have introduced a number of light-trapping strategies. Yet, in the electro-optical calculations we focus on randomly rough textures. This is because (1) structures with optimized rough textures exhibit the photocurrent close to the Lambertian limit; (2) the optimal parameters of the roughness do not depend on the absorber thickness, which allows us to study energy conversion efficiency as a function of thickness without introducing additional degrees of freedom, namely without changing the parameters of the texture; (3) random textures scatter light isotropically, which allows us to generalize the results to a 2D scattering interface into a full 3D system.

5.2. Analytic approach

The first approach to investigate the electro-optical properties of thin-film silicon solar cells with light trapping is the analytic solution of transport equations. To this goal, we develop an electro-optical model that treats a case structure incorporating three main ingredients: (i) the carrier generation rate calculated for nearly Lambertian scattering on the front surface, (ii) bulk recombination, and (iii) surface recombination in presence of increased surface area due to texturing [42].

Full theoretical treatments for silicon solar cells have been developed during the last decades [75–77]. However, none of these treatments systematically investigate the impact of bulk and surface recombinations mediated by defects. These are the dominant losses in real solar cells, and their importance is even larger in thin nanostructured devices.

According to the treatment of Section 2, the carrier generation rate for the case of 2D Lambertian light trapping (neglecting reflection losses) is calculated from the attenuation of the z-component of the Poynting vector (S_z) associated to a given energy E of the solar spectrum:

$$g_{LL}(z,E) = -\left[\frac{1}{S_0}\frac{dS_z}{dz}\right]\phi_{AM1.5}(E)$$
$$= \frac{\alpha_{LL}(R_b e^{-2\alpha_{LL}w}e^{\alpha_{LL}z} + e^{-\alpha_{LL}z})}{1 - R_b e^{-2\alpha_{LL}w}\left(1 - \frac{1}{n_{Si}^2}\right)}\phi_{AM1.5}(E). \tag{9}$$

Here α_{LL} denotes the effective absorption coefficient in the presence of a 2D Lambertian scatterer. This quantity is defined as $\alpha_{LL} = \alpha_{Si}d_{opt}/d$, where α_{Si} is the intrinsic absorption coefficient of silicon, and the fraction represents the optical path enhancement calculated in Section 2. It is worth noticing that the carrier generation rate of Eq. (9) reduces the full 3D electro-optical problem of a patterned device to a much simpler 1D problem depending only on the variable z. This paves the way for an analytic solution of the transport equations, provided scattering from the rough surface approaches the Lambertian limit. In fact, the generation rate of devices with photonic textures such as those investigated in Section 3 may strongly differ from Eq. (9), showing pronounced features due to the field localization in all the three dimensions. As we have appreciated in Section 5.1, this is not the case of the Gaussian rough interfaces investigated in Section 4. The carrier generation rate of these structures closely resembles the one adopted in our model, both in terms of the total absorption and spatial dependence. Since the photocurrent for the optimal rough structures is close to the one calculated for the Lambertian limit, see Fig. 9, we shall readjust the expression given in Eq. (9) and use $g(z,E) = \beta g_{LL}(z,E)$ as the source term for the drift-diffusion equations, with β calculated as the ratio between black solid and red dashed curve in Fig. 9.

We adopt a c-Si n–p junction design, with a thin and heavily doped n-type emitter (80 nm thick) and a lightly doped p-type base. The donor contributions N_d is set to 10^{19} cm^{-3}, and the acceptor concentration N_a to 10^{16} cm^{-3}. The carrier dynamics is modeled under the assumption of the depletion region approximation [78]. A space charge region (SCR) of width w_{scr} settles up across the junction plane, and it is surrounded by two quasi-neutral (qn) regions of widths w_n and w_p. The electrical transport in the SCR is dominated by the electric field, which easily sweeps photogenerated carrier out of the region [78]. For this reason we neglect collection losses in the SCR.

On the other hand, in the qn regions the transport is dominated by diffusion of minority carriers. Recombination in the bulk and at interfaces may strongly affect the collection of the photogenerated carriers. Focusing on the case of minority electrons in the base region, the stationary-state diffusion equation under sunlight may be written as

$$D_n\frac{d^2\Delta n}{dz^2} - \frac{\Delta n}{\tau_n} + g(z,E) = 0, \tag{10}$$

where $D_n = 40$ cm^2/s denotes the electron diffusion constant, Δn is the excess electrons carrier concentration, and τ_n is the effective lifetime in the p-type qn region. This lifetime takes into account all the possible recombination channels in the bulk, namely radiative (which is always negligible), Auger (which is relevant in the n-type material), and Shockley–Read–Hall recombination mediated by defects. When all these contributions are evaluated from material parameters and doping levels, an effective diffusion length for electrons is defined as $L_n = \sqrt{D_n\tau_n}$. This important parameter governs the collection of the photogenerated carriers, and imposes the requirements in terms of material quality to reach high efficiency in thin-film solar cells. A similar treatment holds for holes in the n-type qn region. These are characterized by smaller diffusion constant $D_p = 2$ cm^2/s and, consequently, smaller diffusion length.

Surface recombination of the minority electrons at the rear surface is taken into account in the boundary conditions:

$$\Delta n(z = w_n + w_{scr}) = 0, \tag{11}$$

$$\left.\frac{d\Delta n}{dz}\right|_{z = w_n + w_{scr}} = -\frac{S_{n,eff}}{D_n}\Delta n(z = w), \tag{12}$$

where $S_{n,eff}$ is the effective surface recombination velocity at the back interface. Analogous equations hold for surface recombination of the minority holes at the front surface, and they contain the effective front surface recombination velocity $S_{p,eff}$. In this work we assume the Lambertian scatterer to be at the front surface of the device, hence the back interface is not patterned and $S_{n,eff} \equiv S_n$. The effective SRV at the back is determined only by the concentration of defects at the interface. The effective SRV at the front surface, instead, takes into account also the geometrical surface area increase. The effective surface recombination velocity at the front may be expressed as $S_{p,eff} = K_{area} \cdot S_p$, where K_{area} represents the geometric surface area enhancement. This quantity is of the order of 1.6–1.7 for the optimal photonic lattices presented in Section 3, while it increases up to around 2.5 for the case of interfaces with the 1D Gaussian roughness [73]. Surface recombination is a crucial effect in thin patterned solar cells, and it has to be kept under control by means of effective passivation methods. Using our analytic approach, in the next section we calculate the requirements in terms of S_n and S_p that allow achieving high efficiency.

Combining Eqs. (9) and (10), we calculate the analytic solution for the diffusion equation in the qn regions. The detailed calculation is reported in Ref. [42]. Once the z-dependent excess concentrations are obtained, the contribution to EQE is easily calculated. For the case of electrons in p-type material, this can be written as

$$EQE_{p-type}(E) = \frac{D_n}{\phi_{AM1.5}}\frac{d\Delta n}{dz}\Big|_{z = w_n + w_{scr}}.$$

We further assume ideal carrier collection from the SCR. The corresponding EQE is then calculated directly from the carrier generation rate as

$$EQE_{scr}(E) = \int_{z = w_n}^{z = w_n + w_{scr}} \frac{g(z, E)}{\phi_{AM1.5}(E)}\, dz.$$

When a forward bias V is applied to the junction, majority carriers flow through it, generating a dark current term J_{dark}, which has opposite sign with respect to the short-circuit current. This term is calculated following the standard treatment of semiconductor homojunctions [78]. Once the short-circuit current J_{sc} and the dark current J_{dark} are obtained, the total current flowing through the cell is calculated as the superposition of the two terms: $J(V) = J_{sc} - J_{dark}(V)$.

To conclude, our model allows calculating the main parameters of solar cells, namely the short-circuit current J_{sc}, the open-circuit voltage V_{oc}, and the fill factor FF. The energy conversion efficiency can be written as

$$\eta = FF \times J_{sc} V_{oc} / P_{inc}, \tag{13}$$

and it is investigated over a broad range of absorber thickness and material parameters.

5.3. Numerical approach

The photogeneration profile calculated using RCWA is used as an input for the device simulator. We model the solar cell performance by solving the drift-diffusion equations by means of the FEM with the Silvaco ATLAS device simulator [79]. Both in the optical and electrical calculations we consider two-dimensional structures with a
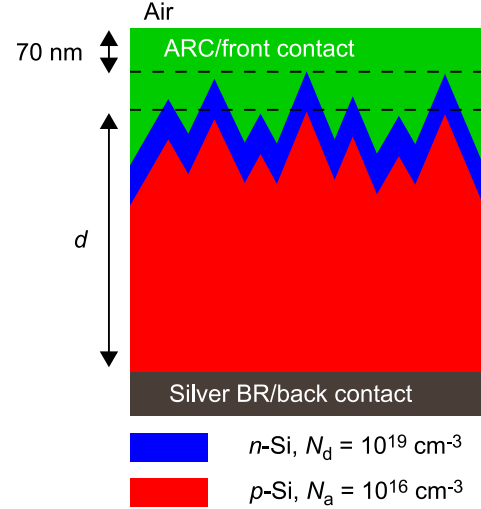

Fig. 12. Structure considered in the FEM simulations. The p–n junction is made of an 80 nm thick n-type layer with donor concentration $N_d = 10^{19}$ cm^{-3}, and p-type layer with acceptor concentration $N_a = 10^{16}$ cm^{-3} [78]. The ARC and silver layers serve as, respectively, front and back contacts. The parameters of the simulated Gaussian texture are the optimal values for c-Si: $\sigma = 300$ nm and $l_c = 160$ nm.

complete randomly rough topography. Yet, rescaling of the photogeneration profile allows us to generalize the results to three-dimensional systems with a 2D random interface.

The structure considered in the FEM simulations is sketched in Fig. 12. It is based on the structure of Fig. 7a, which we have used in the optical simulations. We have added a p–n junction made of an 80 nm thick n-type layer with donor concentration $N_d = 10^{19}$ cm^{-3}, and p-type layer with acceptor concentration $N_a = 10^{16}$ cm^{-3} [78]. The ARC and silver layers serve as, respectively, front and back contacts. Finally, the parameters of the simulated Gaussian texture are the optimal values for c-Si: $\sigma = 300$ nm and $l_c = 160$ nm, as shown in Fig. 8a.

5.4. Results and comparison of the two methods

We start by calculating the basic characteristics of the c-Si solar cells with random textures as a function of the absorber thickness. In Fig. 13 we show the short-circuit current density J_{sc} (a), efficiency η (b), fill factor FF (c), and open-circuit voltage V_{oc} (d). At this point we assume a perfect surface passivation ($S_n = S_p = 0$ cm/s). Moreover, the diffusion lengths related to SRH recombination are taken to be as follows: $L_n = 232$ μm for electrons in the p-type base [8], and $L_p = L_n/10 = 23.2$ μm for holes in the n-type emitter [78]. Analytic results are reported with red symbols and connecting lines, while results from ATLAS simulations are reported with black symbols and connecting lines. Notice that J_{sc} calculated using the analytical model and FEM simulations are nearly identical: this follows from adjusting the Lambertian photogeneration rate used in the analytical model to the photogeneration rate calculated for the roughness.

The relative discrepancy in the calculated efficiency and V_{oc} is of the order of 5% (~1% absolute discrepancy for the efficiency). Yet, the analytic model very well reproduces all the trends. The largest, although still reasonable, discrepancy can be seen for the fill factor. This difference may be caused by two factors: (1) simplifications of the analytical model, as described in Section 5.2; (2) when SRH recombination is considered, the fill factor tends to slightly drop for the textured cells because of the increased area of the junction. This effect cannot be observed in the analytical model, and therefore the model is likely to slightly overestimate the fill factor. Notice, however, that the discrepancy in the
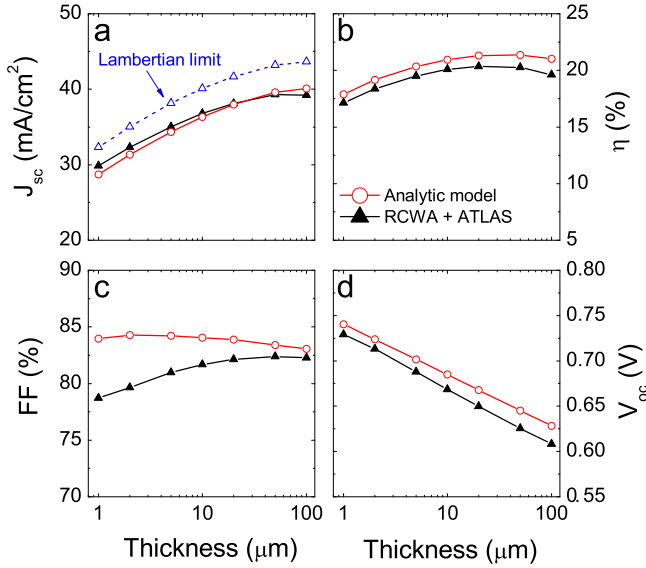
Fig. 13. (a) The main electric parameters for c-Si solar cells with perfect surface passivation ($S_n = S_p = 0$ cm/s): short-circuit current density J_{sc} (a), conversion efficiency η (b), fill factor FF (c), and open-circuit voltage V_{oc} (d). Analytic results are reported with red symbols and connecting lines, while results from ATLAS simulations are reported with black symbols and connecting lines. The Lambertian limit for J_{sc} is reported in (a) with a blue dashed line. The diffusion lengths related to SRH recombination are $L_n = 232$ μm for electrons in the p-type base, and $L_p = 23.2$ μm for holes in the n-type emitter. (For interpretation of the references to color in this figure caption, the reader is referred to the web version of this paper.)

efficiency η is the *smallest* for small thicknesses, as the discrepancy in fill factor is partially compensated by J_{sc} and V_{oc}.

In Fig. 14 we present the energy conversion efficiency as a function of the electron diffusion length L_n and cell thickness. Moreover, in Fig. 15 we show the energy conversion efficiency for the 10 μm thick solar cells as a function of top and bottom surface recombination velocity. In both cases, the analytical model correctly reproduces the trends obtained with the numerical simulations. This agreement holds in a wide range of material parameters and absorber thickness, which indicates that the analytical model is a fast, yet accurate method to simulate textured solar cells. We also note that in the FEM calculations we consider a complete rough topography, and thus the surface increase due to roughness is calculated explicitly. In the analytical model, however, we use an effective surface recombination proportional to the increased surface area, as described in Section 5.2. Therefore, the device physics can be studied in one-dimension without a significant loss of accuracy.

The very good agreement between the results obtained using both methods allows us to draw general conclusions. Both approaches predict the optimal absorber thickness to be in the range 10–30 μm, as shown in Fig. 13b. This optimal thickness results from the opposite trends of current and voltage as a function of thickness, demonstrated in Fig. 13a and d. V_{oc} decreases with increasing thickness, showing that thicker cells are more sensitive to bulk recombination. J_{sc} is compared with the corresponding Lambertian limit, which is calculated assuming a perfect anti-reflection action.

In Fig. 14 we show the dependence of the optimal thickness on the material quality. In our design, the n-type emitter is much thinner than the p-type base. Therefore, as far as bulk recombination is concerned, the cells are likely to be limited by the diffusion length of electrons in the base. As in the previous calculations, the diffusion length of holes in the n-type emitter is 23.2 μm. The optimal thickness for each material quality is indicated with blue symbols (lines are guide to the eye). Notice that the maximum
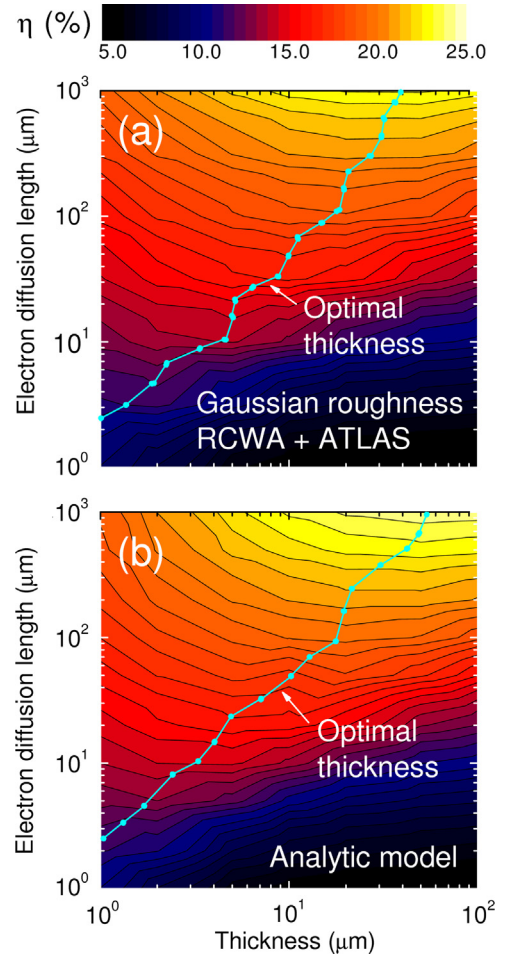

Fig. 14. Energy conversion efficiency for solar cells with perfect surface passivation ($S_n = S_p = 0$ cm/s) as a function of the electron diffusion length L_n and cell thickness. The holes diffusion length in the n-type emitter is set to 23.2 μm. The optimal configurations lie along the blue solid line with symbols. Panel (a) refers to ATLAS calculations, while panel (b) refers to the analytic model. (For interpretation of the references to color in this figure caption, the reader is referred to the web version of this paper.)

efficiency can approach 25% when the electron diffusion length exceeds 1 mm, and the optimal thickness is ~ 40 μm in this case.

The optimal thickness sharply decreases with decreasing material quality (both axis are in log scale). On the one hand, for a very high quality material the optimal thickness approaches bulk values. On the other hand, for a very poor material quality, i.e., for diffusion-limited solar cells, a poor carrier collection efficiency deteriorates the performance of thicker cells, as is demonstrated by the dark area in the bottom part of the plots. Indeed, such a small diffusion length is the case for solar cells based on a-Si, which cannot be thicker than a few hundreds of nanometres.

These conclusions are in agreement with the results reported in Ref. [80], where the measured carrier lifetimes in multicrystalline silicon are used as an input for the PC1D solar cell simulator. This allows one to discuss the energy conversion efficiency as a function of the cell thickness for different material qualities. Also this reference work shows that the optimal thickness significantly decreases with decreasing material quality: the optimal thickness changes from the value well above 150 μm for a very high quality material, to the value below 25 μm for a material with a relatively short carrier lifetime.

Let us now focus on surface recombination. In Fig. 15 one can clearly see an asymmetry, indicating that the cell performance is limited by recombination at the rear (silicon absorber/silver
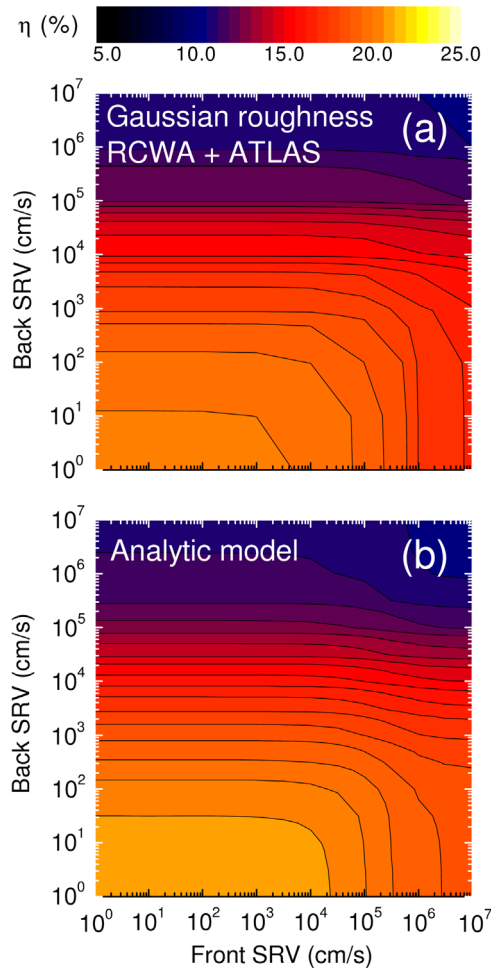
Fig. 15. Energy conversion efficiency for 10 μm thick solar cells as a function of the surface recombination velocities. Diffusions lengths related to SRH recombination are $L_n = 232$ μm for electrons in the p-type base, and $L_p = 23.2$ μm for holes in the n-type emitter. Panel (a) refers to ATLAS calculations, while panel (b) refers to the analytic model.

Fig. 16. Energy conversion efficiency as a function of the back surface recombination velocity and cell thickness. The front SRV is set to $S_p = 10^3$ cm/s. Diffusions lengths related to SRH recombination are $L_n = 232$ μm for electrons in the p-type base, and $L_p = 23.2$ μm for holes in the n-type emitter. Panel (a) refers to ATLAS calculations, while panel (b) refers to the analytic model.

reflector) interface. This follows from taking a solar-cell structure with a thin n-type emitter, thus the carriers are mostly generated in the thick p-type base, where minority electrons recombine at the rear surface. Therefore, as far as surface recombination is concerned, texturing the front surface should not appreciably deteriorate the cell performance.

Having concluded that the cell performance is limited by recombination at the rear interface, let us investigate the dependence on this parameter in more detail. Fig. 16 shows the energy conversion efficiency as a function of back SRV and of the absorber thickness. The front SRV is assumed to be 10^3 cm/s. We note that present-day passivation techniques [81] allow achieving much smaller SRV, of the order or less than 10 cm/s. Yet, based on the analysis above, we concluded that even such a high SRV at the front should not seriously deteriorate the cell performance.

Fig. 16 shows that even in the presence of surface recombination, the conversion efficiency of thin c-Si solar cells can be higher than that of their bulk counterparts. The optimal thickness range is around 20–30 μm. To achieve 20% efficiency, the back SRV should be reduced below 100 cm/s. Moreover, in the optimal thickness range around 20 μm, maximal efficiency requires SRV below 10 cm/s. Such a low SRV at a silicon/metal interface may be challenging. Therefore, the solar cell design should include elements such as a passivation layer or back surface field.
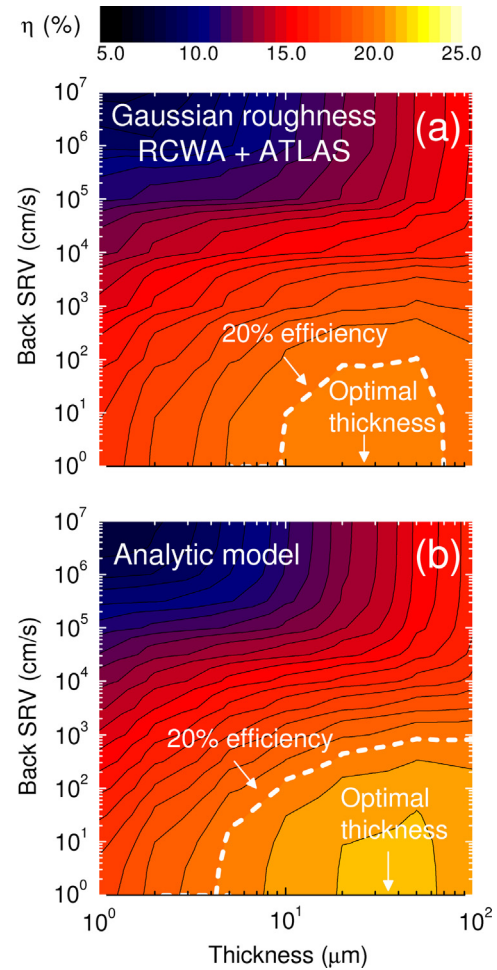
6. Conclusions

Light trapping is crucial to enhance the optical absorption in thin-film solar cells and to reduce the amount of active material required for high efficiency. Two-dimensional photonic crystals realized in the silicon layer yield a substantial increase of the short-circuit current as compared to the unpatterned slab. This is because the incident light is coupled to the guided modes supported by the PhC slab. Moreover, the PhC provides an additional anti-reflection action. However, approaching the Lambertian limit requires the inclusion of disorder in the photonic structures, which is necessary to obtain a broad spectrum of the Fourier components associated with the photonic lattice. This can be achieved by exploiting PhC structures with correlated disorder or by using fully randomly rough surfaces. Considering the requirement of a moderate roughness, which is necessary for the deposition of good-quality silicon on rough substrates, a suitable solution is a hybrid structure consisting of a periodic photonic crystal combined with roughness.

Efficient photovoltaic conversion in thin-film solar cells requires (nearly) Lambertian light trapping and good carrier collection. The solution of the drift-diffusion equations, either with the analytic modeling or with the full-scale numerical simulations, indicates that c-Si solar cells of ∼ 10–40 μm thickness can outperform bulk ones, provided the material quality remains

the same and an efficient light trapping is achieved. The maximum efficiency that can be reached is a function material quality, and it ranges from ~20%, for an electron diffusion length ~230 μm, to ~25% for a diffusion length ≥ 1 mm. These results are robust against surface recombination, provided surface recombination velocity remains below a critical level, which is compatible with present surface passivation techniques. Interestingly, the conversion efficiency is less sensitive to surface recombination at the front interface rather than to the recombination at the rear interface. This conclusion is promising in the view of introducing scattering layers by patterning the front surface.

The analytic model for solving the drift-diffusion equations has been extensively validated against results from full-scale numerical simulations with the Silvaco-ATLAS software. Differences for the energy conversion efficiency are at most around 1–2% absolute in a wide range of parameters. As explained in Section 5, the model can be applied to any photogeneration profile that is close to the Lambertian benchmark, thus it can be employed to calculate the J–V characteristic and conversion efficiency for various photonic structures, even beyond those considered here.

In summary, our calculations indicate that high-efficiency ($\eta > 20\%$) thin-film silicon solar cells are a very challenging but realistic possibility. In principle, even higher efficiencies can be achieved taking a higher c-Si material quality. The general conclusion is that, for a given material quality, a thin-film solar cell with optimal light trapping can be more efficient than its bulk counterpart. The development of high-quality thin-film silicon layers that can serve as PV material for such solar cells based on advanced photonic concepts remains a crucial challenge, which is of great current interest for research in material science. In this regard, it is encouraging that promising steps have been recently reported [4–8] towards this goal.

Acknowledgments

References

[1] H. Sai, K. Saito, N. Hozuki, M. Kondo, Relationship between the cell thickness and the optimum period of textured back reflectors in thin-film microcrystalline silicon solar cells, Appl. Phys. Lett. 102 (5) (2013) 053509.

[2] M. Boccard, C. Battaglia, S. Hänni, K. Söderström, J. Escarré, S. Nicolay, F. Meillaud, M. Despeisse, C. Ballif, Multiscale transparent electrode architecture for efficient light management and carrier collection in solar cells, Nano Lett. 12 (2012) 1344–1348.

[3] K. Söderström, G. Bugnon, F.-J. Haug, S. Nicolay, C. Ballif, Experimental study of flat light-scattering substrates in thin-film silicon solar cells, Sol. Energy Mater. Sol. Cells 101 (2012) 193–199.

[4] V. Depauw, Y. Qiu, K. Van Nieuwenhuysen, I. Gordon, J. Poortmans, Epitaxy-free monocrystalline silicon thin film: first steps beyond proof-of-concept solar cells, Progr. Photovolt.: Res. Appl. 19 (7) (2011) 844–850.

[5] C. Becker, D. Amkreutz, T. Sontheimer, V. Preidel, D. Lockau, J. Haschke, L. Jogschies, C. Klimm, J. Merkel, P. Plocica, S. Steffens, B. Rech, Polycrystalline silicon thin-film solar cells: status and perspectives, Sol. Energy Mater. Sol. Cells 119 (0) (2013) 112–123, doi:http://dx.doi.org/10.1016/j.solmat.2013.05.043.

[6] J. Dore, D. Ong, S. Varlamov, R. Egan, M. Green, Progress in laser-crystallized thin-film polycrystalline silicon solar cells: intermediate layers and metallization, IEEE J. Photovolt. 4 (1) (2014) 33–39. http://dx.doi.org/10.1109/JPHOTOV.2013.2280016.

[7] J. Van Hoeymissen, V. Depauw, I. Kuzma-Filipek, K. Van Nieuwenhuysen, M.R. Payo, Y. Qiu, I. Gordon, J. Poortmans, The use of porous silicon layers in thin-film silicon solar cells, Phys. Status Solidi A 208 (6) (2011) 1433–1439.

[8] J.H. Petermann, D. Zielke, J. Schmidt, F. Haase, E.G. Rojas, R. Brendel, 19%-efficient and 43 μm−thick crystalline Si solar cell from layer transfer using porous silicon, Progr. Photovolt.: Res. Appl. 20 (1) (2012) 1–5.

[9] G. Bauhuis, P. Mulder, E. Haverkamp, J. Huijben, J. Schermer, 26.1% thin-film GaAs solar cell using epitaxial lift-off, Sol. Energy Mater. Sol. Cells 93 (9) (2009) 1488–1491.

[10] B.M. Kayes, H. Nie, R. Twist, S.G. Spruytte, F. Reinhardt, I.C. Kizilyalli, G. S. Higashi, 27.6% conversion efficiency, a new record for single-junction solar cells under 1 sun illumination, in: 37th IEEE Photovoltaic Specialists Conference (PVSC), IEEE, 2011, pp. 000004–000008.

[11] I. Repins, M.A. Contreras, B. Egaas, C. DeHart, J. Scharf, C.L. Perkins, B. To, R. Noufi, 19· 9%-efficient ZnO/CdS/CuInGaSe₂ solar cell with 81· 2% fill factor, Progr. Photovolt.: Res. Appl. 16 (3) (2008) 235–239.

[12] P. Jackson, D. Hariskos, E. Lotter, S. Paetel, R. Wuerz, R. Menner, W. Wischmann, M. Powalla, New world record efficiency for Cu (In, Ga) Se2 thin-film solar cells beyond 20%, Progr. Photovolt.: Res. Appl. 19 (7) (2011) 894–897.

[13] J.H. Heo, S.H. Im, J.H. Noh, T.N. Mandal, C.-S. Lim, J.A. Chang, Y.H. Lee, H.-j. Kim, A. Sarkar, M.K. Nazeeruddin, et al., Efficient inorganic–organic hybrid heterojunction solar cells containing perovskite compound and polymeric hole conductors, Nat. Photonics 7 (6) (2013) 486–491.

[14] M. Liu, M.B. Johnston, H.J. Snaith, Efficient planar heterojunction perovskite solar cells by vapour deposition, Nature 501 (7467) (2013) 395–398.

[15] C. Heine, R.H. Morf, Submicrometer gratings for solar energy applications, Appl. Opt. 34 (14) (1995) 2476–2482.

[16] S. Hava, M. Auslender, Design and analysis of low-reflection grating microstructures for a solar energy absorber, Sol. Energy Mater. Sol. Cells 61 (2) (2000) 143–151.

[17] P. Bermel, C. Luo, L. Zeng, L.C. Kimerling, J.D. Joannopoulos, Improving thin-film crystalline silicon solar cell efficiencies with photonic crystals, Opt. Express 15 (25) (2007) 16986–17000.

[18] I. Prieto, B. Galiana, P.A. Postigo, C. Algora, L. Martínez, I. Rey-Stolle, Enhanced quantum efficiency of ge solar cells by a two-dimensional photonic crystal nanostructured surface, Appl. Phys. Lett. 94 (19) (2009) 191102.

[19] S. Zanotto, M. Liscidini, L.C. Andreani, Light trapping regimes in thin-film silicon solar cells with a photonic pattern, Opt. Express 18 (5) (2010) 4260–4274.

[20] J. Buencuerpo, L.E. Munioz-Camuniez, M.L. Dotor, P.A. Postigo, Optical absorption enhancement in a hybrid system photonic crystal—thin substrate for photovoltaic applications, Opt. Express 20 (104) (2012) A452–A464.

[21] X. Meng, V. Depauw, G. Gomard, O. El Daif, C. Trompoukis, E. Drouard, C. Jamois, A. Fave, F. Dross, I. Gordon, C. Seassal, Design, fabrication and optical characterization of photonic crystal assisted thin film monocrystalline-silicon solar cells, Opt. Express 20 (104) (2012) A465–A475.

[22] F.-J. Haug, K. Söderström, A. Naqavi, J. Li, C. Ballif, Super-Lambertian photocurrent-generation in solar cells with periodically textured interfaces, Appl. Phys. Lett. 103 (13) (2013) 131108.

[23] O. Isabella, S. Solntsev, D. Caratelli, M. Zeman, 3-d optical modeling of thin-film silicon solar cells on diffraction gratings, Progr. Photovolt.: Res. Appl. 21 (1) (2013) 94–108.

[24] C. Martella, D. Chiappe, P. Delli Veneri, L. Mercaldo, I. Usatii, F. Buatier de Mongeot, Self-organized broadband light trapping in thin film amorphous silicon solar cells, Nanotechnology 24 (22) (2013) 225201.

[25] R. Peretti, G. Gomard, L. Lalouat, C. Seassal, E. Drouard, Absorption control in pseudodisordered photonic-crystal thin films, Phys. Rev. A 88 (5) (2013) 053835.

[26] G. Gomard, R. Peretti, E. Drouard, X. Meng, C. Seassal, Photonic crystals and optical mode engineering for thin film photovoltaics, Optics Exp. 21 (103) (2013) A515–A527.

[27] A. Abass, C. Trompoukis, S. Leyre, M. Burgelman, B. Maes, Modeling combined coherent and incoherent scattering structures for light trapping in solar cells, J. Appl. Phys. 114 (3) (2013) 033101.

[28] M. Burresi, F. Pratesi, K. Vynck, M. Prasciolu, M. Tormen, D.S. Wiersma, Two-dimensional disorder for broadband, omnidirectional and polarization-insensitive absorption, Optics Exp. 21 (102) (2013) A268–A275.

[29] K. Jäger, M. Fischer, R.A. van Swaaij, M. Zeman, Designing optimized nano textures for thin-film silicon solar cells, Opt. Express 21 (104) (2013) A656–A668.

[30] S. Wiesendanger, M. Zilk, T. Pertsch, F. Lederer, C. Rockstuhl, A path to implement optimized randomly textured surfaces for solar cells, Appl. Phys. Lett. 103 (13) (2013) 131115.

[31] N. Sahraei, K. Forberich, S. Venkataraj, A.G. Aberle, M. Peters, Analytical solution for haze values of aluminium-induced texture (ait) glass superstrates for a-Si:H solar cells, Opt. Express 22 (101) (2014) A53–A67.

[32] E. Yablonovitch, Statistical ray optics, J. Opt. Soc. Am. 72 (7) (1982) 899–907.

[33] M.A. Green, Lambertian light trapping in textured solar cells and light-emitting diodes: analytical solutions, Progr. Photovolt.: Res. Appl. 10 (4) (2002) 235–241.

[34] A. Ingenito, O. Isabella, M. Zeman, Experimental demonstration of 4n2 classical absorption limit in nanotextured ultrathin solar cells with dielectric omnidirectional back reflector, ACS Photonics 1 (3) (2014) 270–278. http://dx.doi.org/10.1021/ph4001586.

[35] M. Ernst, R. Brendel, Lambertian light trapping in thin crystalline macroporous Si layers, Phys. Status Solidi: Rapid Res. Lett. 8 (3) (2014) 235–238. http://dx.doi.org/10.1002/pssr.201308294.

[36] A. Deinega, S. Eyderman, S. John, Coupled optical and electrical modeling of solar cell based on conical pore silicon photonic crystals, J. Appl. Phys. 113 (2013) 224501.

[37] O. Isabella, H. Sai, M. Kondo, M. Zeman, Full-wave optoelectrical modeling of optimized flattened light-scattering substrate for high efficiency thin-film silicon solar cells, Progr. Photovolt: Res. Appl. 22 (6) (2014) 671–689. http://dx.doi.org/10.1002/pip.2314.

[38] M.G. Deceglie, V.E. Ferry, A.P. Alivisatos, H.A. Atwater, Design of nanostructured solar cells using coupled optical and electrical modeling, Nano Lett. 12 (6) (2012) 2894–2900.

[39] G. Gomard, X. Meng, E. Drouard, K. El Hajjam, E. Gerelli, R. Peretti, A. Fave, R. Orobtchouk, M. Lemiti, C. Seassal, Light harvesting by planar photonic crystals in solar cells: the case of amorphous silicon, J. Opt. 14 (2) (2012) 024011.

[40] A. Ingenito, O. Isabella, S. Solntsev, M. Zeman, Accurate opto-electrical modeling of multi-crystalline silicon wafer-based solar cells, Sol. Energy Mater. Sol. Cells 123 (2014) 17–29.

[41] M. Peters, M. Rüdiger, B. Bläsi, W. Platzer, Electro-optical simulation of diffraction in solar cells, Opt. Express 18 (104) (2010) A584–A593.

[42] A. Bozzola, P. Kowalczewski, L. Andreani, Towards high efficiency thin-film crystalline silicon solar cells: the roles of light trapping and non-radiative recombinations, J. Appl. Phys. 115 (9) (2014) 094501.

[43] P. Kowalczewski, A. Bozzola, M. Liscidini, L. Claudio Andreani, Light trapping and electrical transport in thin-film solar cells with randomly rough textures, J. Appl. Phys. 115 (19) (2014), doi:http://dx.doi.org/10.1063/1.4876223.

[44] R. Lo Savio, M. Galli, M. Liscidini, L.C. Andreani, G. Franz, F. Iacona, M. Miritello, A. Irrera, D. Sanfilippo, A. Piana, F. Priolo, Photonic crystal light emitting diode based on Er and Si nanoclusters co-doped slot waveguide, Appl. Phys. Lett. 104 (12) (2014), doi:http://dx.doi.org/10.1063/1.4869751.

[45] M. Galli, D. Gerace, K. Welna, T.F. Krauss, L. O'Faolain, G. Guizzetti, L.C. Andreani, Low-power continuous-wave generation of visible harmonics in silicon photonic crystal nanocavities, Opt. Express 18 (25) (2010) 26613––26624. http://dx.doi.org/10.1364/OE.18.026613.

[46] L. Carroll, D. Gerace, I. Cristiani, S. Menezo, L.C. Andreani, Broad parameter optimization of polarization-diversity 2d grating couplers for silicon photonics, Opt. Express 21 (18) (2013) 21556–21568. http://dx.doi.org/10.1364/OE.21.021556.

[47] L. Carroll, D. Gerace, I. Cristiani, L.C. Andreani, Optimizing polarization-diversity couplers for Si-photonics: reaching the −1 db coupling efficiency threshold, Opt. Express 22 (12) (2014) 14769–14781. http://dx.doi.org/10.1364/OE.22.014769.

[48] Z. Yu, A. Raman, S. Fan, Fundamental limit of light trapping in grating structures, Opt. Express 18 (103) (2010) A366–A380.

[49] A. Bozzola, M. Liscidini, L.C. Andreani, Broadband light trapping with disordered photonic structures in thin-film silicon solar cells, Progr. Photovolt.: Res. Appl., doi:http://dx.doi.org/10.1002/pip.2385.

[50] A. Bozzola, M. Liscidini, L.C. Andreani, Photonic light-trapping versus Lambertian limits in thin film silicon solar cells with 1d and 2d periodic patterns, Opt. Express 20 (102) (2012) A224–A244.

[51] C.S. Schuster, A. Bozzola, L.C. Andreani, T.F. Krauss, How to assess light trapping structures versus a Lambertian scatterer for solar cells? Opt. Express 22 (102) (2014) A542–A551.

[52] D. Whittaker, I. Culshaw, Scattering-matrix treatment of patterned multilayer photonic structures, Phys. Rev. B 60 (4) (1999) 2610.

[53] M. Liscidini, D. Gerace, L.C. Andreani, J. Sipe, Scattering-matrix analysis of periodically patterned multilayers with asymmetric unit cells and birefringent media, Phys. Rev. B 77 (3) (2008) 035324.

[54] X. Meng, V. Depauw, G. Gomard, O.E. Daif, C. Trompoukis, E. Drouard, C. Jamois, A. Fave, F. Dross, I. Gordon, C. Seassal, Design, fabrication and optical characterization of photonic crystal assisted thin film monocrystalline-silicon solar cells, Opt. Express 20 (S4) (2012) A465–A475. http://dx.doi.org/10.1364/OE.20.00A465.

[55] C. Trompoukis, O. El Daif, V. Depauw, I. Gordon, J. Poortmans, Photonic assisted light trapping integrated in ultrathin crystalline silicon solar cells by nanoimprint lithography, Appl. Phys. Lett. 101 (10) (2012) 103901.

[56] E.D. Palik, Handbook of Optical Constants of Solids, Academic, Orlando, 1985.

[57] A. Gombert, K. Rose, A. Heinzel, C. Zanke, B. Bläsi, V. Wittwer, Antireflective submicrometer surface-relief gratings for solar applications, Sol. Energy Mater. Sol. Cells 54 (1) (1998) 333–342.

[58] A. Herman, C. Trompoukis, V. Depauw, O. El Daif, O. Deparis, Influence of the pattern shape on the efficiency of front-side periodically patterned ultrathin crystalline silicon solar cells, J. Appl. Phys. 112 (2012) 103107.

[59] T.C. Choy, Effective Medium Theories: Principles and Applications, Oxford University Press, Oxford, 1999.

[60] O. Stenzel, Effective Medium Theories: Principles and Applications, Springer, Berlin, 2005.

[61] C. Battaglia, C.-M. Hsu, K. Sderstrm, J. Escarr, F.-J. Haug, M. Charrire, M. Boccard, M. Despeisse, D.T.L. Alexander, M. Cantoni, Y. Cui, C. Ballif, Light trapping in solar cells: can periodic beat random? ACS Nano 6 (3) (2012) 2790–2797 arXiv:http://pubs.acs.org/doi/pdf/10.1021/nn300287j, doi:http://dx.doi.org/10.1021/nn300287j.

[62] E.R. Martins, J. Li, Y. Liu, J. Zhou, T.F. Krauss, Engineering gratings for light trapping in photovoltaics: the supercell concept, Phys. Rev. B 86 (4) (2012) 041404.

[63] E.R. Martins, J. Li, Y. Liu, V. Depauw, Z. Chen, J. Zhou, T.F. Krauss, Deterministic quasi-random nanostructures for photon control, Nat. Commun. 4 (2013) 2665.

[64] A. Oskooi, P.A. Favuzzi, Y. Tanaka, H. Shigeta, Y. Kawakami, S. Noda, Partially disordered photonic-crystal thin films for enhanced and robust photovoltaics, Appl. Phys. Lett. 100 (18) (2012) 181110.

[65] F. Pratesi, M. Burresi, F. Riboli, K. Vynck, D.S. Wiersma, Disordered photonic structures for light harvesting in solar cells, Opt. Express 21 (S3) (2013) A460–A468. http://dx.doi.org/10.1364/OE.21.00A460.

[66] A. Naqavi, F.-J. Haug, C. Ballif, T. Scharf, H.P. Herzig, Limit of light coupling strength in solar cells, Appl. Phys. Lett. 102 (2013) 131113.

[67] I. Simonsen, Optics of surface disordered systems, Eur. Phys. J. Spec. Top. 181 (1) (2010) 1–103.

[68] T. Lanz, B. Ruhstaller, C. Battaglia, C. Ballif, Extended light scattering model incorporating coherence for thin-film silicon solar cells, J. Appl. Phys. 110 (3) (2011) 033111.

[69] D. Dominé, F.-J. Haug, C. Battaglia, C. Ballif, Modeling of light scattering from micro- and nanotextured surfaces, J. Appl. Phys. 107 (4) (2010) 044504.

[70] V. Freilikher, E. Kanzieper, A. Maradudin, Coherent scattering enhancement in systems bounded by rough surfaces, Phys. Rep. 288 (1) (1997) 127–204.

[71] C. Rockstuhl, S. Fahr, K. Bittkau, T. Beckers, R. Carius, F.-J. Haug, T. Söderström, C. Ballif, F. Lederer, Comparison and optimization of randomly textured surfaces in thin-film solar cells, Opt. Express 18 (103) (2010) A335–A341.

[72] P. Kowalczewski, M. Liscidini, L.C. Andreani, Engineering Gaussian disorder at rough interfaces for light trapping in thin-film solar cells, Optics Lett. 37 (23) (2012) 4868–4870.

[73] P. Kowalczewski, M. Liscidini, L.C. Andreani, Light trapping in thin-film solar cells with randomly rough and hybrid textures, Opt. Express 21 (105) (2013) A808–A820.

[74] O. Isabella, J. Krč, M. Zeman, Modulated surface textures for enhanced light trapping in thin-film silicon solar cells, Appl. Phys. Lett. 97 (10) (2010) 101106.

[75] T. Tiedje, E. Yablonovitch, G.D. Cody, B.G. Brooks, Limiting efficiency of silicon solar cells, IEEE Trans. Electron Devices 31 (5) (1984) 711–716.

[76] M.A. Green, Limits on the open-circuit voltage and efficiency of silicon solar cells imposed by intrinsic auger processes, IEEE Trans. Electron Devices 31 (5) (1984) 671–678.

[77] M.A. Green, Limiting efficiency of bulk and thin-film silicon solar cells in the presence of surface recombination, Progr. Photovolt.: Res. Appl. 7 (4) (1999) 327–330.

[78] J. Nelson, The Physics of Solar Cells, Imperial College Press, London, 2003.

[79] Silvaco Atlas, URL ⟨http://www.silvaco.com/⟩.

[80] B. Michl, M. Kasemann, W. Warta, M.C. Schubert, Wafer thickness optimization for silicon solar cells of heterogeneous material quality, Phys. Status Solidi (RRL)—Rapid Res. Lett. 7 (11) (2013) 955–958.

[81] M. Otto, M. Kroll, T. Käsebier, R. Salzer, A. Tünnermann, R.B. Wehrspohn, Extremely low surface recombination velocities in black silicon passivated by atomic layer deposition, Appl. Phys. Lett. 100 (19) (2012) 191603.